Tectonophysics 766 (2019) 302–325

Contents lists available at ScienceDirect

Tectonophysics

journal homepage: www.elsevier.com/locate/tecto

Kinematic, flexural, and thermal modelling in the Central Andes: Unravelling age and signal of deformation, exhumation, and uplift

Victoria M. Buford Parks*, Nadine McQuarrie

University of Pittsburgh, Pittsburgh, PA, United States of America

ARTICLE INFO

Keywords:
Central Andes
Fold thrust belt
Foreland basin
Altiplano
Thermokinematic modelling

ABSTRACT

Quantifying age, rate, and lateral variation of deformation and exhumation in convergent systems relies on integration of geologic map patterns, ag, and locations of reset thermochronometer systems, and synorogenic sediment distribution. The central Bolivian Andes provide an ideal location to examine the influence of variations in shortening and stratigraphic architecture on the structural evolution of the mountain range due to differential age and rates of shortening and distinct sedimentary basin geometries along strike. To quantify age and rate of shortening, we link thermokinematic modelling of sequentially deformed, forward-modelled, balanced cross-sections to synorogenic and thermochronologic histories. The preserved basin history in the Altiplano and Eastern Cordillera argues for an early fold-and-thrust belt located in the now-Western Cordillera, with subsequent propagation of shortening eastward around 40–50 Ma. Flexural modelling incorporating isostasy and erosion requires multiple basement thrust sheets with 35–97 km of displacement. A temporally evolving effective elastic thickness, as well as imposed subsidence in the foreland and uplift in the hinterland, is required to reproduce the surface geology, increase Subandean foreland basin depth, limit Altiplano sedimentation, and facilitate Altiplano uplift to modern elevation. Thermokinematic modelling is compatible with initiation of deformation at 50–40 Ma in a marked increase in Subandean velocities from ~5.5 to 8–10 mm/yr from ~12–10 Ma to present. Out-of-sequence thrusting at the westernmost limit of the Subandes is required to match measured young and partially reset zircon helium ages. Out-of-sequence faulting is supported by high Ksn values, indicative of active uplift, and was likely promoted by the abrupt eastern edge of the Paleozoic basin rocks, which limited forward propagation of structures, and/or increased erosion due to focused precipitation. Our results highlight the importance of incorporating detailed structural modelling in differentiating the geometry, kinematics, and timing of deformation to reproduce thermochronologic ages and basin histories.

1. Introduction

The Andes mountains, formed in response to compressional strain driven by the subducting Nazca plate, is the modern archetype of a retro-arc fold-thrust-belt-foreland basin (FTB-FB) system. The Central Andes, located in northern Chile, Argentina, Bolivia, and southern Peru is the widest portion of the mountain belt. Both proposed and observed variations in timing and magnitude of deformation, exhumation, and uplift across the Central Andes have generated questions about the processes of lithospheric deformation, and delamination and crustal growth, which are key to understanding the impact of Andean deformation on society from both natural hazards and hydrocarbon extraction. Although results and models from one geographic location are often depicted as applying to the Central Andes as an entity, the map-view expression and style of structures, stratigraphy exposed at the surface, age and magnitude of exhumation, and uplift show a lateral variability along and across strike (Fig. 1) (Anderson et al., 2017; Barnes et al., 2008; Garzione et al., 2014; Lease et al., 2016; McQuarrie, 2002; Saylor and Horton, 2014; Sundell et al., 2019). Map patterns of rocks and visible structures are commonly used to understand the extent of subsurface faulting, as well as infer locations of lateral structures (Boyer and Elliot, 1982; Kley, 1996). Additionally, integrative work incorporating well-mapped geology, structural interpretations, rock samples, and thermal and climate modelling can be used to help understand lithospheric processes and evolution (Garzione et al., 2017; Horton, 2018a). While many previous studies have attempted to

Abbreviations: OOS, out-of-sequence; FTB, fold-thrust-belt; FB, foreland basin; AP, Altiplano; EC, Eastern Cordillera; IAZ, Interandean Zone; SA, Subandes; AFT, Apatite fission track; ZHe, zircon (U-Th)/He; EET, elastic thickness

* Corresponding author.
E-mail address: vmbparks@gmail.com (V.M. Buford Parks).

https://doi.org/10.1016/j.tecto.2019.06.008
Received 11 January 2019; Received in revised form 3 June 2019; Accepted 12 June 2019
Available online 24 June 2019

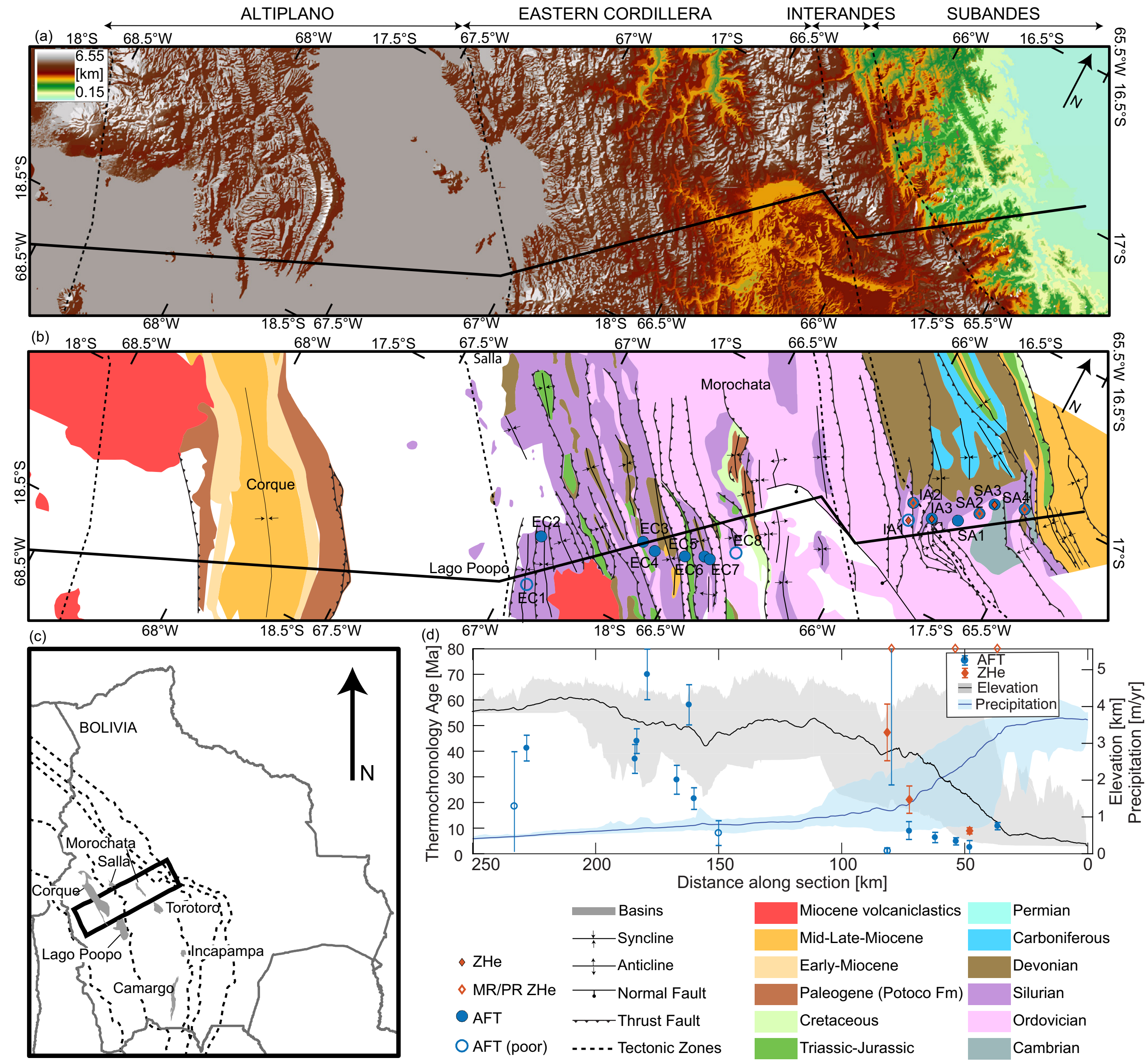

Fig. 1. Area Map with (a) Elevation, (b) geology and thermochronology sample locations, (c) Regional map highlighting basins and localities referenced in text, and (d) precipitation, elevation and thermochronometer ages across the cross-section; shaded area is the min to max range, with the solid line being the average. Open blue circles indicate samples with poor data quality (Table 1); open orange diamonds indicate mixed/partial reset ZHe samples. Dashed lines in (a-c) are tectonogeomorphic zones.

delineate structural relationships, age of initiation of shortening, and magnitude and timing of deformation, differing interpretations of the existing data and associated uncertainties has led to conflicting interpretations, such as predominantly west-verging surface and basement structures at the western edge of the Eastern Cordillera (Armijo et al., 2015; Müller et al., 2002) or east-verging (Anderson et al., 2017; McQuarrie, 2002), differing age and rate of SA shortening (Anderson et al., 2018; Gubbels et al., 1993; Lease et al., 2016; McQuarrie et al., 2005; Oncken et al., 2006, 2012; Rak et al., 2017), and the correlation (or lack thereof) between shortening and uplift (Barnes and Ehlers, 2009; Garzione et al., 2008, 2017; Lamb, 2011). Our goal with this contribution is to quantitatively link the structural evolution of the FTB at 18°S with the resulting cooling ages and foreland basin history to evaluate permissible geometries, kinematics, and rates. The process of linking kinematic models of deformation derived from balanced cross-sections to advection–diffusion thermal models in order to calculate the evolving subsurface temperatures and predict cooling ages has been explored recently by several research groups (Almendral et al., 2015; Castelluccio et al., 2015; Chapman et al., 2017; Erdös et al., 2014; Gilmore et al., 2018; McQuarrie and Ehlers, 2015; Mora et al., 2015; Rak et al., 2017). We incorporate fault motion, isostasy, and erosion predicted by a geologic cross-section with the predicted thermal evolution in order to characterize the relationship between fault geometry, timing and magnitude of shortening, exhumation, and sedimentation (Gilmore et al., 2018; McQuarrie and Ehlers, 2015; Rak et al., 2017).

Although published cross-sections along the Bolivian Andes show many similarities, there are also pronounced differences in the geometry and location of basement structures and the proposed kinematics that link basement and surface deformation, exhumation and sedimentation (Anderson et al., 2018; Armijo et al., 2015; Baby et al., 1997; McQuarrie, 2002; McQuarrie et al., 2005, 2008a; Müller et al., 2002; Rak et al., 2017). In addition, across Bolivia, age and magnitude of exhumation gleaned from apatite fission track (AFT) and apatite and zircon (U-Th)/He (AHe, ZHe) thermochronology show significant variations, with initiation of exhumation in the EC at 45-50 Ma near both 15–17°S and 18°S, but not until ~36–42 Ma at 19.5–21°S (Anderson et al., 2018; Barnes et al., 2008, 2012). Interandean zone (IAZ) exhumation in the north began > 25 Ma with a second pulse of exhumation ~15 Ma to present (Barnes et al., 2006). In central Bolivia, rapid IAZ exhumation was likely between 18 and 6 Ma, but exhumation could have initiated as early as 40–50 Ma (Barnes et al., 2012; Eichelberger et al., 2013). A similar exhumation history exists for the IAZ of southern Bolivia: a potential ~25–17 Ma start with rapid exhumation between 20 and 5 Ma (Anderson et al., 2018; Barnes et al., 2008). In the northern SA, exhumation and deformation started ~19–20 Ma (Barnes et al., 2008; Rak et al., 2017). In the central Bolivian Subandes (SA), exhumation initiated at 14 ± 4 Ma (Barnes et al., 2012; Eichelberger et al., 2013), and in the south, SA exhumation can start potentially as early as 18 Ma (Barnes et al., 2008; Calle et al., 2018), but reset AFT and AHe ages range from 11 to 6 Ma and 6–2 Ma respectively (Anderson et al., 2018; Lease et al., 2016). The majority of AP sedimentation in the Corque syncline finished around ~10 Ma, with low rates of accumulation until ~5 Ma. Altiplano deformation initiated between ~15 and 10 Ma and continued to ~5 Ma. (Garzione et al., 2006; Lamb, 2011; Lamb and Hoke, 1997; McQuarrie and DeCelles, 2001). Additionally, the San Juan del Oro paleosurface post-dates all EC shortening and is dated at ~10 Ma (Gubbels et al., 1993).

Deformation rates depend on the timing of onset of deformation as well as the magnitude of shortening. Shortening estimates in the central Andes range from ~200 to 400 km (Anderson et al., 2017; Baby et al., 1995, 1997; Eichelberger et al., 2015; Gotberg et al., 2010; Kley, 1996; McQuarrie, 2002; McQuarrie et al., 2008a; Müller et al., 2002; Perez et al., 2016). With an onset of deformation at ~50 Ma, these shortening magnitudes equate to 4–8 mm/yr at constant rates. While the magnitude of shortening and onset of deformation can provide an initial long-term shortening rate, shortening rates in the Central Andes are likely variable through time (Anderson et al., 2018; Echavarria et al., 2003; Elger et al., 2005; McQuarrie et al., 2005, 2008a; Rak et al., 2017; Uba et al., 2009). Active shortening in the Andes, recorded by GPS, is currently accommodated in the SA at ~9–13 mm/yr (Brooks et al., 2011), notably higher than the long term average of 4–8 mm/yr, though Quaternary estimates of convergence rates range from 7 to 11 mm/yr (Echavarria et al., 2003; Uba et al., 2009).

The growing suite of structural, sedimentological, geomorphological, and thermochronological data through the central Andes provides an opportunity to evaluate if and how along strike changes in exhumation and sedimentation are related to proposed along strike changes in the geometries of structures and the rates at which they move. We assess the importance of along strike change by evaluating a sequentially-deformed, isostatically balanced, thermo-kinematic model of the central Bolivian Andes near 18°S (Fig. 1) and compare our results to a similar modelling approach from 15 to 17°S and published geometries and rates from 19.5 to 21°S. The combined modelling techniques in this study allow us to evaluate the geometry and kinematic sequence of faulting, permissible timing and rates of deformation, and evaluate the validity of a published cross-section.

2. Geologic background

2.1. Central Andes

There are several distinct tectonogeomorphic zones in the Andes; from west to east, these are: Western Cordillera (WC), Altiplano (AP), Eastern Cordillera (EC), Interandean Zone (IAZ), and Subandes (SA). The AP is a low-relief, high-elevation (~3.7 km), internally drained basin consisting of up to 12 km thick Cretaceous and Tertiary synorogenic sedimentary rocks derived initially from sources west of the AP, with upper portions being derived from the EC (DeCelles and Horton, 2003; Horton, 2005; Horton et al., 2001, 2002). The EC and IAZ host a thick (~15 km) continuous succession of Paleozoic marine siliciclastic rocks, and a discontinuous section (2–4 km) of nonmarine Carboniferous through Cretaceous rocks (Sempere, 1995) deformed in narrow anticlines and synclines. These zones encompass a bivergent thrust belt system that reaches 6.4 km in elevation in the EC and decreases in elevation towards the east with significant decreases in both topographic and structural elevation in the IAZ and SA. Both the EC and IAZ are argued to be uplifted as the result of basement thrusts faults (Kley, 1996; Kley et al., 1999; McQuarrie, 2002). The SA is the actively deforming portion of the Andean fold-and-thrust belt (FTB), whose thrust faults carry Cambrian through Cretaceous rocks and fold 4–7 km of Tertiary foreland basin sedimentary rocks (Baby et al., 1995; McQuarrie, 2002).

2.2. Shortening estimates and crustal thickness

Early estimates of shortening in the Central Andes documented shortening amounts ranging from 191 to 231 km (Baby et al., 1995, 1997; Kley, 1996) that emphasized well-defined structures and detailed shortening estimates in the eastern portions of the system. A wealth of detailed mapping in the western portion of the eastern Cordillera, including improved stratigraphic relationships and fault geometries, have generated larger estimates of total shortening ranging from 265 to 326 km (Anderson et al., 2017; Eichelberger et al., 2013; McQuarrie, 2002; McQuarrie et al., 2008a; McQuarrie and DeCelles, 2001; Müller et al., 2002; Rak et al., 2017; and references therein). Estimates of crustal shortening are directly related to the potential for accumulated crustal thicknesses. In Bolivia, the crust ranges from 35 km thick in the foreland to approximately 60 km under the EC and 65 + km thick under the AP (Ryan et al., 2015). The Andean plateau, at 3 + km elevation, is largely in Airy isostatic equilibrium, though shortening estimates and volumetric analyses shown that the uniformly thick crust may be a function of crustal flow from regions of high shortening and over-thickening to areas of lower crustal shortening (Eichelberger et al., 2015).

The balanced cross-section used in this study (original from McQuarrie, 2002) argues that the Paleozoic shortening is balanced at depth by long, ~10 km thick, east-verging basement thrust sheets, where slip along a mid-crustal detachment near the brittle-ductile transition is transferred to upper décollement horizons in the Paleozoic section. The emplacement of these thrust sheets up and over their associated footwall ramps impose a first-order control on topographic uplift, focused exhumation, and thus the pattern of thermochronologic ages (McQuarrie and Ehlers, 2015, 2017; Rak et al., 2017).

2.3. Regional thermochronology

Thermochronometer cooling ages are a function of the timing, magnitude, and rate of exhumation, and thus directly related to the paths the rocks take to the surface due to the influences of both vertical and lateral transport along faults on the rate and magnitude of exhumation (Ehlers and Farley, 2003; Gilmore et al., 2018; McQuarrie and Ehlers, 2017; Rak et al., 2017). Thus, subsurface structures impart the first order pattern to cooling ages and can be used to verify or invalidate a cross-section (Gilmore et al., 2018; McQuarrie and Ehlers, 2015). By requiring sequentially deformed balanced cross-sections to produce predicted cooling ages that match measured thermochronologic data, the modelled evolution of a mountain belt can be adjusted to more accurately depict the structural evolution of the area.

Previously published low-temperature thermochronometer samples in the FTB in Bolivia (Anderson et al., 2017; Barnes et al., 2006, 2008;

Table 1
Thermochronologic data used in this study. Sample IDs correspond to Fig. 1. All AFT ages are pooled ages. P(χ^2) > 5% and concordant. P(χ^2) < 5% discordant and may not represent one geologic event. n = number of grains measured. MR = Mixed reset; PR = Partial Reset. Sources: [1]Barnes et al., 2012; [2]Eichelberger et al., 2013; [3]Lease et al., 2016.

Sample ID	Sample #	Latitude	Longitude	Elevation [m]	Fm age	AFT age [Ma] 2σ error	AFT n	AFT P(χ^2)	ZHe corrected age [Ma]
AL1	B815–5	−18.49	−68.67	3950	Camb	83.5 ± 20.8[1]	13[1]	0.1[1]	
AL2	B815–1	−18.48	−68.67	4144	Camb	43.2 ± 13.6[1]	24[1]	59.2[1]	
EC1	05JBBL070	−18.00	−66.95	3874	Sil	17.7 ± 21.2[1]	2[1]	75[1]	
EC2	05JBBL071	−17.88	−67.02	3684	Sil	40.3 ± 5[1]	38[1]	50[1]	
EC3	05JBBL067	−17.71	−66.66	3998	Sil	43.0 ± 4.8[1]	39[1]	0[1]	
EC3	Bol10–201	−18.26	−66.17	4150	O	36.1 ± 5.6 [2]	100[2]	11[2]	
EC4	B611–5	−17.72	−66.61	3850	Dv	68.9 ± 9.8[1]	37[1]	0[1]	
EC5	66–7	−17.69	−66.51	3600	Ord	28.0 ± 5.6[1]	31[1]	59.8[1]	
EC6	05JBBL065	−17.66	−66.45	3559	Dv	57.1 ± 7.8[1]	39[1]	0.01[1]	
EC7	05JBBL064	−17.66	−66.43	3209	Sil/Ord	20.7 ± 4.1[1]	37[1]	6.1[1]	
EC8	05JBBL062	−17.60	−66.36	2761	Ord	7.3 ± 4.8[1]	5[1]	0[1]	
IA1	05JBBL060	−17.23	−65.89	3154	Ord	0.5 ± 1[1]	2[1]	0[1]	47.1 ± 11[3]
IA2	05JBBL059	−17.17	−65.90	2772	Ord	126 ± 100[1]	19[1]	85[1]	MR[3]
IA3	05JBBL058	−17.19	−65.82	1787	Sil/Ord	8.1 ± 3.6[1]	27[1]	0[1]	21.0 ± 5.3[3]
SA1	05JBBL056	−17.16	−65.74	1762	Ord	5.6 ± 2[1]	34[1]	65[1]	PR[3]
SA2	05JBBL055	−17.10	−65.68	882	Ord	4.1 ± 1.4[1]	34[1]	35[1]	MR[3]
SA3	05JBBL054	−17.06	−65.65	611	Camb	1.8 ± 2.6[1]	14[1]	100[1]	8.9 ± 1.2[3]
SA4	05JBBL052	−17.02	−65.55	410	Sil/Ord	10.0 ± 1.4[1]	30[1]	0.02[1]	

Eichelberger et al., 2013; Gillis et al., 2006; Lease et al., 2016) have been interpreted as the result of deformation-induced erosional exhumation (Barnes et al., 2012; Eichelberger et al., 2013; McQuarrie et al., 2005, 2008b). We limit the thermochronometer data used in this study to those located within 75 km of the cross-section to include all potentially relevant cooing ages and exclude significant lateral variability in structure and timing of exhumation captured by the data (Fig. 1, Table 1) (Barnes et al., 2012; Eichelberger et al., 2013; Lease et al., 2016), and are projected along structure to the cross-section line. Cooling ages and sample locations are shown in Fig. 1. Apatite fission track (AFT) pooled ages and zircon (U-Th)/He (ZHe) cooling ages are shown with 2σ error (Fig. 1c, Table 1). AFT, which has a typical closing temperature of ~110 ± 10 °C and a partial annealing range of 60–110 °C (Donelick et al., 2005), are typically reported as pooled ages when concordant (P(χ^2) > 5%), and as mean ages when discordant (P(χ^2) < 5%), as the pooled age may not reflect a distinct geologic event when samples are over-dispersed. However, the AFT data from Barnes et al., 2012, is only available as pooled ages, regardless of whether they are concordant or discordant, as a result of the non-Poissonian counting process used in the LA-ICPMS (Barnes et al., 2006, 2008, 2012). Ages classified as "poor" had n < 10 grains measured. Despite these limitations on the quality of data, we use all published AFT data equally. The AFT ages with n > 10 grains range from 1.8 to 8.1 Ma in the SA and IAZ. In the EC, the youngest measured cooling ages have low grain counts (7.3 Ma, n = 5; 17.7 Ma, n = 2), and the youngest age with n > 10 grains is 20.7 Ma (n = 37). From east to west, measured AFT ages broadly increase to 68.9 Ma, then decrease to 17.7 Ma at the western most edge of the EC (Barnes et al., 2012; Eichelberger et al., 2013). ZHe cooling ages, with a typical closure temperature of ~180 ± 10 °C and partial retention zone of ~130–200 °C (Guenthner et al., 2013; Reiners, 2005; Reiners et al., 2002, 2004; Wolfe and Stockli, 2010), increase in age westward from 8.9 to 47.1 Ma over the SA and IAZ (Lease et al., 2016) (Fig. 1c).

At 18°S, measured AFT cooling ages and associated modelling (HeFTy) argues for onset of EC exhumation around 50–45 Ma (Samples EC3, EC2) (Barnes et al., 2012), as the earliest possible deformation in the EC, set by the age of the earliest fully reset thermochronometric age. Sample EC3 and EC2 have AFT ages 43.0 ± 4.8 Ma and 40.3 ± 5 (respectively) and modelling indicates onset of rapid cooling at 54–45 Ma and 41–25 Ma. Samples with older pooled ages (EC4 and EC6) are best modelled with onset of rapid cooling at 45–35 Ma (EC6) and 32–18 Ma (EC4) (Barnes et al., 2012). EC deformation lasts until ~25 Ma (EC7) (Barnes et al., 2012).

Previous authors suggest that IAZ exhumation initiated as early as ~30 Ma with an acceptable fit, or 14–21 Ma with good fit, and continued exhumation through 2 Ma is supported by HeFTy modelling with AFT and ZHe data (sample IA2) (Barnes et al., 2012; Lease et al., 2016). The pooled AFT ages of samples IA1 (0.5 ± 1 Ma) and IA3 (8.1 ± 3.6 Ma) are a function of the continuing, younger exhumation. The mixed and partially reset ZHe ages are likely a function of sample depth (IA2, SA2, SA1) (Lease et al., 2016) and/or presence around the closure temperature for an extended period of time (IA2) (Barnes et al., 2012). The best estimate for onset of exhumation is 6 ± 2 Ma from integrated age-depth profiles (Lease et al., 2016), with rapid SA exhumation from 7 to 3 Ma supported by AFT and ZHe HeFTy modelling (Barnes et al., 2012; Lease et al., 2016).

2.4. Regional sedimentology

2.4.1. Altiplano

The sedimentary section preserved in the AP records the transition from pre-Andean sedimentation to an early foreland basin (Horton et al., 2001). This includes the ~200–600 m thick El Molino Formation (Fm.), a regionally extensive marginal marine sequence dated at ~72 Ma that marks the end of marine conditions in the AP (Horton et al., 2001; Sempere et al., 1997). This is topped by a mid-Paleocene, eastward-sourced 50–300 m thick Santa Lucia Fm. overlain by 20–100 m of Potoco paleosols indicative of 15–20 Myr of reduced (< 10 mm/yr) sediment accumulations during mid-Paleocene to middle Eocene (Horton et al., 2001). The paleosols are overlain by an upper Eocene through Oligocene phase of rapid fluvial aggradation (sedimentation rates up to 500 m/Myr) of the ~3000–6500 m thick Potoco Fm (Horton et al., 2001). This transition is interpreted as foredeep migration over initial forebulge deposits. The Potoco Fm. is broken into the westward-sourced ~3500–4000 m thick, upper Eocene, Lower Potoco Fm., and the poorly-dated, eastern- and western-derived ~2500 m thick Upper Potoco Fm., dated at ~23–24 Ma via K-Ar/Ar on biotite (Horton et al., 2001; Kennan et al., 1995), and thus requires active deformation and exhumation in the EC prior to this time (Horton et al., 2001; McQuarrie et al., 2005). However, 40–50 Ma cooling ages from the EC from 15 to 18°S argue that deformation migrated into the EC by 40 Ma at the latest (Barnes et al., 2012; Eichelberger et al., 2013; Gillis et al., 2006; McQuarrie et al., 2008a; Rak et al., 2017) which should have provided a new sediment source for the Altiplano from the

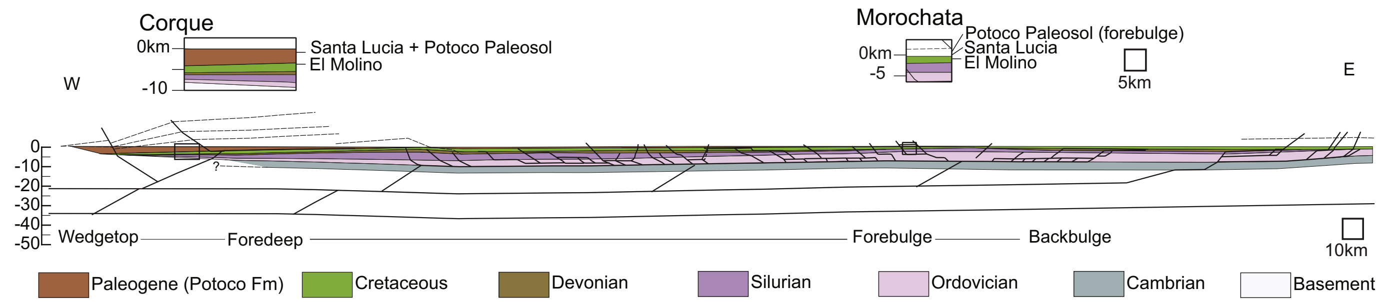

Fig. 2. Initial *Move* Model Setup showing initial flexural state of lithosphere and sediment thicknesses at initiation of model. No vertical exaggeration. Stratigraphy insets at 2× Cross-Section Scale.

east (McQuarrie et al., 2005), that are not seen in the lower Potoco Fm (Horton et al., 2001). Preservation of that eastern derived material rests on the distance between the EC uplift and the modern Altiplano basin, as well as in the magnitude of sedimentary material that was recycled as the EC continues to shorten (Rak et al., 2017). The uppermost units of the section are the eastward-derived, early Miocene Coniri/lower Totora Fms. (~1000 m thick) and up to 5000 m of volcanic-rich deposits of the upper Totora/Crucero Fms., late Miocene through Quaternary in age (Horton et al., 2001; Lamb, 2011).

2.4.2. Eastern Cordillera

Sedimentology of the EC intermontane basins preserved in the Camargo, Incapampa, Torotoro, and Morochata synclines (located throughout the EC from 21.5°S to 17.5°S, Fig. 1c) is also interpreted to record the transition from backbulge to forebulge to foredeep (Horton, 2005). These rocks include the Paleocene to early Eocene, eastward-sourced Santa Lucia Fm. topped by ~80 m thick paleosols of the Early Eocene Impora Fm., the overlying eastward-sourced Cayara Fm., and the westward-sourced, > 2 km thick Camargo Fm. with a clear EC source (DeCelles and Horton, 2003; Horton, 2005). The interpreted depositional environments require that a proto-FTB, initially active west of the AP, produced the backbulge and forebulge depozones identified in the AP and EC. Deformation jumped eastward in the Eocene, encapsulating the AP as a piggyback basin and provided the sediment source for the Camargo Fm. (DeCelles and Horton, 2003; Horton, 2005; McQuarrie et al., 2005). Deformation in the far-west EC is also recorded in the onlapping sedimentary basins in the Lago Poopo (18°S) and Salla (17.5°S) regions. These depocenters contain synorogenic sediments sitting directly on Silurian-Devonian age rocks. The synorogenic sedimentary rocks show growth strata and are dated at 28 Ma (Salla; (Gillis et al., 2006; Leier et al., 2010)) and ~25 Ma (Lago Poopo; (Lamb and Hoke, 1997)) requiring erosion of Devonian and younger rocks prior to 25 Ma (Leier et al., 2013; McQuarrie, 2002) with modest amounts of shortening post 29–25 Ma. The flexural kinematic modelling shown in this paper predicts both magnitude of erosion and flexural basin formation for each increment of modelled shortening that we can directly compare to measured cooling ages and basin stratigraphy.

3. Approach/methods

In order to quantitatively link the geometry and kinematics of deformation with the associated sedimentation and thermal histories to derive the age and signal of exhumation in this region, we created a sequentially deformed, flexurally loaded, forward modelled cross-section, as well as thermo-kinematic models for four different kinematic variations.

3.1. Kinematic modelling

McQuarrie (2002) published a balanced cross-section through central Bolivia at 18°S. Using the 2D Kinematic Module in the modelling software *Move* (Midland Valley), the restored section was deformed sequentially using the Fault Parallel Flow Algorithm and using the passive wedge option for emplacement of the basement thrust sheets underneath the EC backthrust belt. Exact amounts of shortening on each fault are modified to best match the geometry of the structures using the imposed algorithms and differ slightly from the balanced cross-section (in McQuarrie, 2002) due to the limited ability of the software to precisely replicate structures and deformation processes documented in the region (e.g. McQuarrie and Davis, 2002).

3.2. Sequential deformation and isostasy

3.2.1. Model setup

To replicate proposed foreland basin geometry and deposition in the AP and EC, we used *Move2015.2* (Midland Valley) to model an initial scenario wherein 200 km of shortening in the WC produced a migrating flexural basin. Modelled accommodation space created by flexure permitted 1.1–3.2 km of back bulge, forebulge, and initial foredeep deposition in the AP, (representing the El Molino, Santa Lucia, and some of the basal Potoco), and ~1.3 km of backbulge and forebulge deposition in the eastern EC, (the Santa Lucia and Impora formations) (Fig. 2), similar to the method in (Rak et al., 2017). Because we evaluate a suite of different ages (40, 45, 50 Ma) for initiation of EC deformation, the initial deposition of the westward-derived ~40 Ma Potoco Formation (Horton et al., 2001) could predate (models that start < 40 Ma), coincide with (model start of ~40 Ma), or postdate (models that start > 40 Ma) early deformation in the EC. This beginning scenario is not thermally modelled and is used simply to create initial model conditions that are consistent with the proposed locations and magnitude of forebulge and backbulge depozones that are interpreted to precede deformation in the EC (DeCelles and Horton, 2003; McQuarrie et al., 2005).

Our methods for sequential deformation and isostasy build on previous work (Gilmore et al., 2018; McQuarrie and Ehlers, 2015, 2017; Olsen et al., 2019; Rak et al., 2017) and was initially accomplished in ~20 km deformational increments (Fig. 3). Following each deformation step, the flexural-isostatic load is calculated from the difference between the deformed topography and the previously undeformed topographic surface using the *Move2015.2* 2D Decompaction module that employs a bulk density, and a spatially uniform effective elastic thickness (EET) (Fig. 3c, Table 2). For thrust loading, the bulk density is assigned to the space that defines the load (difference between the deformed topography and the previously undeformed topographic surface) and is hereafter referred to as the load density (ρ_{load}).The equations used in *Move* to model the flexural response follow Turcotte and Schubert (1982) to compute the deflection of the lithosphere caused by the load. Flexural-kinematic modelling is an iterative process, and EET, load and sediment density, and erosion angle (typically between 1 and 3°) are varied systematically for a suite of models to optimize the fit of the final model to the observed surface geology,

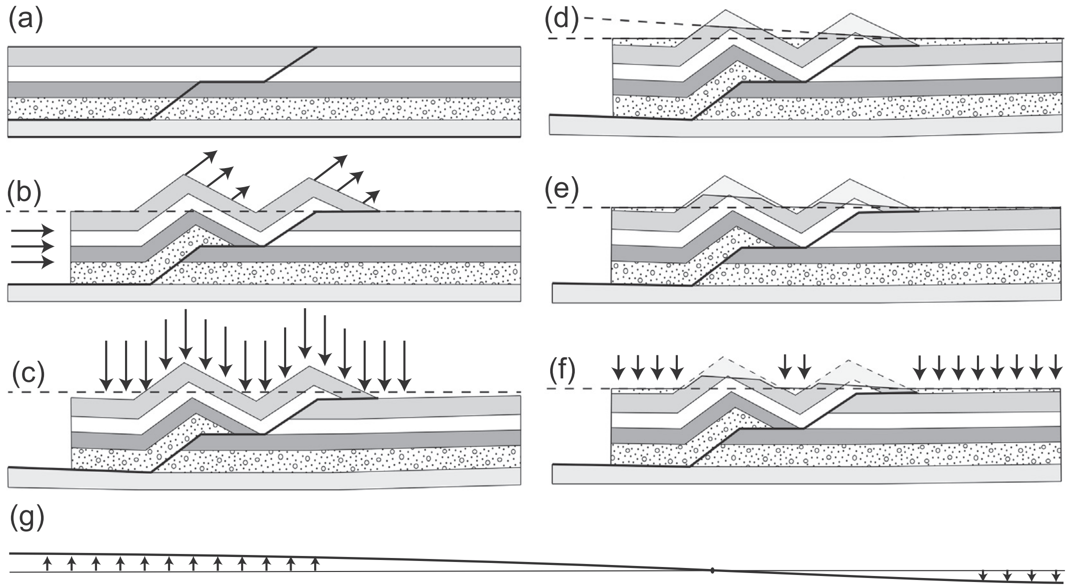

Fig. 3. Schematic of kinematic-flexural modelling steps. (a) undeformed state, (b) deformation along fault, (c) loading due to isostasy, (d) erosion at critical angle, (e) erosional unloading, (f) loading due to sedimentation, and (g) general shape of imposed uplift and subsidence.

Table 2
Move model parameters for all kinematic variations tested.

Parameter		Value
ρ_{load}		2500 kg/m^3 [a]
ρ_{sed}		2100 kg/m^3
ρ_{mantle}		3300 kg/m^3
Young's modulus		70 GPa
Shortening/step		~6 km
EET during deformation in:	E. EC/IAZ	40 km
	W. EC	15–45 km
	AP	100 km
	AP + SA	100 km
	SA	100 km
Imposed uplift and subsidence	Under AP	+7.2 km
	Under IAZ	−2.7 km
	Under SA	−1.3 km

[a] On steps with only AP loading, ρ = 2300 kg/m^3 was used.

foreland basin depth, sedimentary history, and surface thermochronology (Gilmore et al., 2018; McQuarrie and Ehlers, 2015, 2017; Olsen et al., 2019; Rak et al., 2017). A flexural basin in both the hinterland and foreland is created response to this loading. The previous elevation horizon, representing the erosional or depositional surface across the model, subsides in these basins in response to the isostatic load. These horizons create a modelled stratigraphy though time. A new eroded surface was modelled following critical taper theory, such that the topography was eroded at a specified angle, α, from the deformation front. The new topographic profile followed the existing topography below the westward-increasing angle while any rocks exposed above the new topographic profile were eroded (Fig. 3d). Regions that subside below 0 km are filled with sediments up to 0 km. Sedimentation does not occur above 0 km with the exception of the AP, where sedimentation is allowed in topographic lows above sea level, of up to 0.5 km of sediment accumulation per step. The preservation and accumulation of sedimentation is traced throughout the model in these flexurally created basins and can be compared to chronostratigraphic constraints. Elevations are restricted to 6.5 km in the eastern EC, 5 km in the western EC, and 4 km in the AP based on the upper limits of the modern landscape. Westward facing slopes were allowed to increase to 45° when structural deformation locally rotated the topographic slope. Isostatic unloading of eroded material was calculated following the same algorithm, density, and elastic thickness as the loading step, which typically results in ~0.1–0.5 km of additional erosion (Fig. 3e) due to isostatic rebound. In order to preserve strata in the western EC (backthrust belt), the calculated topographic surface was preserved and was not eroded in the post-isostatic unloading step. This is consistent with a dry, less erosive climate. Sediment loading was also included to account for the accumulation of sediments in foreland and hinterland flexural basins. Using a sediment-appropriate density, calculations are performed with the same elastic thickness to calculate the load associated with the new basin fill (Fig. 3f; Table 2).

The synorogenic sedimentation modelled by the process described above created a basin that is 10 km thicker than that preserved in the Altiplano (i.e. overfilled) with a topographic surface that remained at 0 km elevation throughout the model. Additionally, deformation-induced loading throughout the model process described above does not produce the necessary subsidence of the foreland basin, resulting in basin that was ~1 km too shallow. To correct AP overfill and SA underfill, imposed uplift (over the AP) and subsidence (over the SA) was incorporated by applying a long-wavelength sinusoidal curve and unfolding the section to this new shape, with maximum subsidence occurring under the SA and maximum uplift occurring under the eastern edge of the AP in order to match modern EC elevation and foreland basin depths (Fig. 3g) (Rak et al., 2017). This adjustment is required because the *Move* model isostatically accounts for only thrust and sediment loading and erosional unloading. It does not account for the accumulation of mid- to lower-crustal thickness inherently associated with the modelled upper-crustal shortening. A range of both documented and inferred geodynamic processes in the Andes affect accumulation of crustal rock (and thus thicknesses), accumulation of lithosphere, and surface elevations through time and these cannot be flexurally modelled. Dynamic subsidence related to viscous coupling of the mantle wedge can increase the foreland basin load, thus increasing the accommodation space available, particularly in cordilleran orogens (Catuneanu, 2004; DeCelles, 2012; Gurnis, 1993; Mitrovica et al., 1989; Rak et al., 2017). Uplift related to mantle delamination has been invoked to account for rapid elevation change of the Andean Plateau (Garzione et al., 2006), and arguments against flexural support of the plateau, such as Airy isostasy due to a thick crustal column (Beck et al., 1996) and thickening of the EC and AP due to lower crustal flow from east to west (Eichelberger et al., 2015; Isacks, 1988; Lamb, 2011), have been proposed as necessary to maintain AP and EC elevations in the absence of active structurally induced uplift (Rak et al., 2017).

3.3. Thermal modelling

A 0.5 km × 0.5 km grid of unique points was placed over the extent of the undeformed flexural-kinematic model (following McQuarrie and Ehlers, 2015). The grid extends to the bottom of the basement thrust décollement and above 0 km in locations where basins form. The grid extends a total of 780 km, including 65 km beyond the cross-section extent at the eastern and western edges to ensure that the thermal model boundary conditions do not influence the thermal gradient near sample locations. The grid was deformed following the same steps as the final successful flexural model, but with ~10 km sequential deformation steps (to more accurately capture the behavior and evolution of loading, unloading, and the kinematics of the fault geometry). The grid and surface topography were exported at each step. These deformed grids produce vectors of displacement at each grid point that are converted to velocity fields by differencing the locations and assigning an age at each step. These velocities and topographies, in combination with thermal parameters, were input into a modified version of the thermal advection-diffusion software *Pecube* (Braun, 2002, 2003; McQuarrie and Ehlers, 2015; Whipp et al., 2009) (Table 3). This modified version of *Pecube* solves the three-dimensional heat transport equation to simulate the evolving crustal thermal field based on the input thermal parameters and velocity fields to derive the time-temperature (t-T) history of exhumed rocks based on their transport paths (McQuarrie and Ehlers, 2015; Rak et al., 2017). Model-predicted ages at the surface for individual thermochronometer systems uses thermochronometer kinetics described in Ehlers (2005) and Braun (2003). Measured AFT and ZHe ages, and the associated HeFTy models, were not used as an input to *Pecube* thermal models. The predicted cooling ages from Pecube are compared directly to measured ages. Matches between measured and modelled ages were identified if the modelled age, with a ± 1 Ma and ± 2 km error, fell within any portion of the measured age and its error. The match of measured to modelled cooling ages are used to constrain which thermal and velocity parameters provide the best fit.

The thermal model extends to a base depth of 110 km with a temperature of 1300 °C, and up to the surface, where the temperature at sea level is 23 °C (Santa Cruz yearly average), and decreases at 5.3 °C/km, the mean lapse rate measured in Bolivia (Gonfiantini et al., 2001). The model holds the temperature at the surface and base constant. The thermal model is permitted 50 Myr to equilibrate crustal temperatures prior to initiation of Andean shortening. We tested two different methods for modelling the crustal thermal profile; the first applies constant radiogenic heat production (A_o = 0.6–1.0 μW/m^3) to the entire crustal section, while the second applies a surface radiogenic heat production (A_o = 3.0–4.0 μW/m^3) that decreases exponentially with depth (e-folding depths of 12 or 15 km).

Table 3
Pecube thermokinematic modelling properties.

Parameter	Input value
Crustal volumetric heat production (A_o)	0.5–4.0 μW/m^3
e-folding depth (ef)	0, 12, 15 km
Thermal conductivity	2.5 W/m/K
Specific heat	800 J/kg/K
Model base	110 km
Temperature at base	1300 °C
Temperature at surface	23 °C
Atmospheric lapse rate	5.3 °C/km
Kinematic grid spacing	0.5 km × 0.5 km
Displacement increment	~8–10 km
Model domain	780 km × 110 km × 5 km
Horizontal node spacing	0.5 km
Vertical node spacing	1.0 km
Model start time (thermal initiation)	100 Ma

4. Results

4.1. Flexural-kinematic model

Using the kinematic sequence portrayed in McQuarrie (2002), we produced over 40 different flexural-kinematic models in which EET, erosion angle, density, kinematics, and geometry were varied. Initial models tested with space- and time-invariant EET (four models, a through d, with temporally uniform EETs = 25, 30, 40, and 50 km, respectively) and density (ρ_{load} = 2900 kg/m^3), without calculating the load of sediments filling the basin. Results from these flexural-kinematic models that produced a dramatic mismatch between observed data and model results are described below but not depicted in figures. Models a and b resulting in overfilling the AP (by ~10 km) and underfilling of the FB (only ~2 km thick). Models c and d had over-erosion of the Paleozoic sedimentary cover in the EC that occurred during the initial 10–30 km of basement thrust sheet motion, as well as underfilling of the SA basin (~3 km thick) and overfilling of the AP (by ~5–7 km). Thus, this kinematic sequence (from McQuarrie, 2002) was refined to split the second basement thrust sheet into two thrust sheets, to prevent over-erosion of the Paleozoic sedimentary cover. The location of the new basement footwall ramp was chosen such that the material overlying it had the deepest erosion level in the Paleozoic section. However, this new split basement only resolved over-erosion of the Paleozoic cover, and subsequent models with time-invariant EET still resulted in overfilling of the AP and underfilling of the SA. Thus, we modelled an evolving EET that started at low values (15–40 km, Table 2) at the initiation of the model, which gradually increased to 50 km throughout deformation in the backthrust belt. Once deformation in the AP initiates, an EET of 100 km is maintained throughout the model (the maximum in *Move2015.2*). The EET evolution presented here was necessary to accurately reproduce the cross-section and may be representative of changing lithospheric strength such as the transition from an initial weak, faulted lithosphere to one supported by the Brazilian craton.

We iteratively tested another series of flexural-kinematic models which evaluated a suite of temporally varying EET values as well as different load and sediment densities with the goal of matching the surface geology and basin depths (AP and SA), with the most critical constraint to not over erode strata that is currently exposed across the EC and replicating the modern AP and EC elevations. Flexural models with a split basement thrust sheet and time-varying EET still could not replicate the modern AP elevations, nor the SA basin depths. The modern AP elevations were unable to be replicated because once active deformation in the AP ceases, there is no further mechanism of uplift, and the AP rapidly sinks to at or below 0 km elevation. Imposed uplift (500 m increments) was implemented across the AP and western EC to provide non-flexural support after AP deformation ceases. Imposed subsidence (100 m increments) provided SA accommodation space. The final successful models increase EET from 15 to 100 km, have a load density of 2500 kg/m^3, sediment density of 2100 kg/m^3, and a total of up to 7.2 km of imposed uplift under the AP and western EC and up to 1.3 km of imposed subsidence under the SA (Fig. 11f, Table 2).

We then evaluated a series of kinematic scenarios with the goal of replicating the measured thermochronology data in addition to matching the mapped surface geology and measured basin depths (Fig. 4); all kinematic models have the same EET, density, and imposed uplift and subsidence (Table 2). All models have ~2 km of OOS motion in far-west EC (to match Lago Poopo erosion and sedimentation history). The models varied in their SA kinematics and include: (1) in-sequence deformation, (2) ~3 km of OOS on IAZ/SA boundary fault, (3 & 4) ~15 km of OOS motion on IAZ/SA boundary, that is accommodated by two different sequences of faulting.

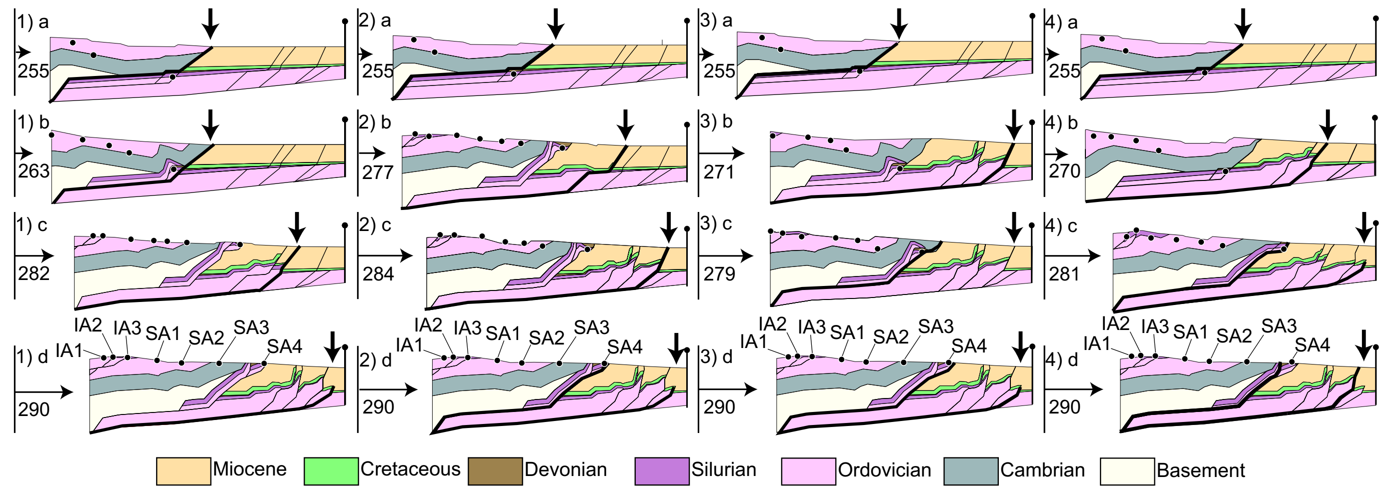

Fig. 4. Kinematic Variations tested, (1) a-d Model 1– in sequence, (2) a-d Model 2- some OOS motion on IAZ/SA boundary, (3) a-d Model 3 –some OOS on IAZ/SA boundary fault, (4) a-d Model 4– Same amount of OOS as Model (3) but on different IAZ/SA boundary fault. (a-d) Vertical arrow tracks deformation front through time. Bolded fault is most recently active. Black circles are thermochronology sample locations through time. Large numbers next to arrows on left indicate total amount of shortening [km]. (d) Thermochronology sample names.

4.2. Modelled cooling ages

4.2.1. Sequential deformation and development of modelled thermochronology ages

In order to understand the effect of geometry on modelled thermochronology ages, we model the evolution of the FTB and predicted cooling ages through time. For samples with sufficient burial temperatures, the earliest possible cooling age is a function of when structures initiate, elevate topography, and facilitate exhumation. If burial was not enough to fully reset the sample, then the partially reset age will be between the age of the detrital sample and the age of exhumation that accompanies motion on a given structure. The initial model uses a constant rate of shortening, approximately 5.7 mm/yr, to accommodate 287 km of shortening since 50 Ma (Fig. 5). This allows for the initiation of deformation to predate the oldest fully reset cooling ages in the EC. The model runs from 100 Ma to present and allows an initial 50 Myr for the thermal model to equilibrate crustal temperatures; at the time deformation initiates (t = 50 Ma, Fig. 5a), all thermochronometers are 50 Ma in age. Samples that have already cooled through the closure temperature age with the passage of model time, such that the unreset AFT ages, present at the surface at t = 42 Ma, are ~58 Ma (Fig. 5b). At t = 42 Ma, shortening is accommodated from west to east through a series of décollement levels. First, exhumation in the WC is driven by uplift over a basement ramp 0 near ~650 km (Fig. 5b); this basement ramp in the WC drives loading in the AP and provides a source of uplift and exhumation to produce western-derived sediments found in the AP. Moving eastward, slip is transferred on a décollement approximately ~20 km in depth to the next basement ramp, where the basement thrust sheet 1 drives exhumation of the overlying cover and exposes reset predicted AFT ages over the basement ramp (470–490 km, Fig. 5b). The modelled reset ages form a characteristic U-shaped cooling pattern, with the youngest ages pinned at the ramp (~0.5 Ma at ~490 km) and gently increasing in age in the direction of transport to the tip of the hangingwall ramp (~5 Ma at ~470 km), where there is a break in age and the modelled ages at the surface are no longer reset (Fig. 5b) (McQuarrie and Ehlers, 2015, 2017; Rak et al., 2017). Subsidence due to isostatic loading forms a flexural basin in front of and behind basement thrust sheet 1 (~440 km, ~510 km), that fills with accumulated sediments and buries the far-western EC (Fig. 5b). Slip is transferred further eastward on a décollement at the base of the Ordovician section, approximately 10 km in depth. Duplexing of the Silurian age rocks and shortening in the upper Paleozoic section and the associated exhumation that accompanies it exposes partially reset AFT from ~110–160 km (Fig. 5b). As each individual fault only has a small amount of motion on it (~2 km), there is not enough deformation to induce exhumation of fully reset AFT ages; the youngest partial reset age exposed (~38 Ma at 160 km) is on the hinterland (west) side of the duplex, as this has the deepest exhumation, and tapers to an unreset age of ~60 Ma at 110 km (Fig. 5b).

At t = 27 Ma (Fig. 5c), uplift and exhumation in the WC is ongoing due to active basement ramp 00, which continues to provide sediments to the AP. Slip along the basement décollement has propagated further east to the next basement ramp where emplacement of basement thrust sheet 2 and associated erosion exhumes fully reset AFT ages in a broad-wavelength, U-shaped cooling pattern. The youngest AFT ages, ~0.5 Ma, are pinned at the ramp at ~360 km, and gently increase in age eastward to the tip of the hangingwall ramp to ~20 Ma, near ~275 km (Fig. 5c). The locus of deformation, and thus isostasy, jumped forward with the emplacement of basement thrust 2. The rocks initially overlying this ramp experienced the highest amount of exhumation in the Paleozoic cover, eroding Cretaceous through upper Silurian rocks. The deepest exhumation is seen in the reset ZHe cooling signal, which is ~22 Ma near the tip of the hangingwall ramp (~275 km), due to erosional exhumation over the basement ramp, and at ~360 km, driven by both the basement ramp uplift and OOS motion in the far-west EC Paleozoic section (Fig. 5c). As motion continues over this basement ramp, flexural subsidence increases, deepening the décollement and creating flexural basins in front of and behind the ramp, promoting AP and foreland basin sedimentation all the way into the IAZ and burying the previously deformed and exhumed strata near ~110–160 km. This flexural subsidence dampens the amount of subsequent erosional exhumation over the ramp, limiting the extent of reset ZHe ages to only above the hangingwall and footwall ramps of basement thrust sheet 2 (250–350 km) (Fig. 5c). In front of basement sheet 2, westward-propagating shortening in the Paleozoic section provides a mix of partial reset and unreset ages driven by small amounts of deformation on individual faults.

At t = 24 Ma (Fig. 5d), uplift in the WC due to basement ramp 00 is ongoing, continuing to provide a western sediment source for the AP. Basement thrust sheets 1 and 2 are no longer actively deforming, as deformation propagated eastward again with the emplacement of basement thrust sheet 3, producing reset AFT ages between 200 and 220 km (Fig. 5d). Because rocks in this region had already undergone deformation-induced exhumation which exposed partially reset AFT ages (Fig. 5c, ~210 km), the AFT signal due to emplacement of basement thrust sheet 3 has a broad-wavelength pattern driven by the

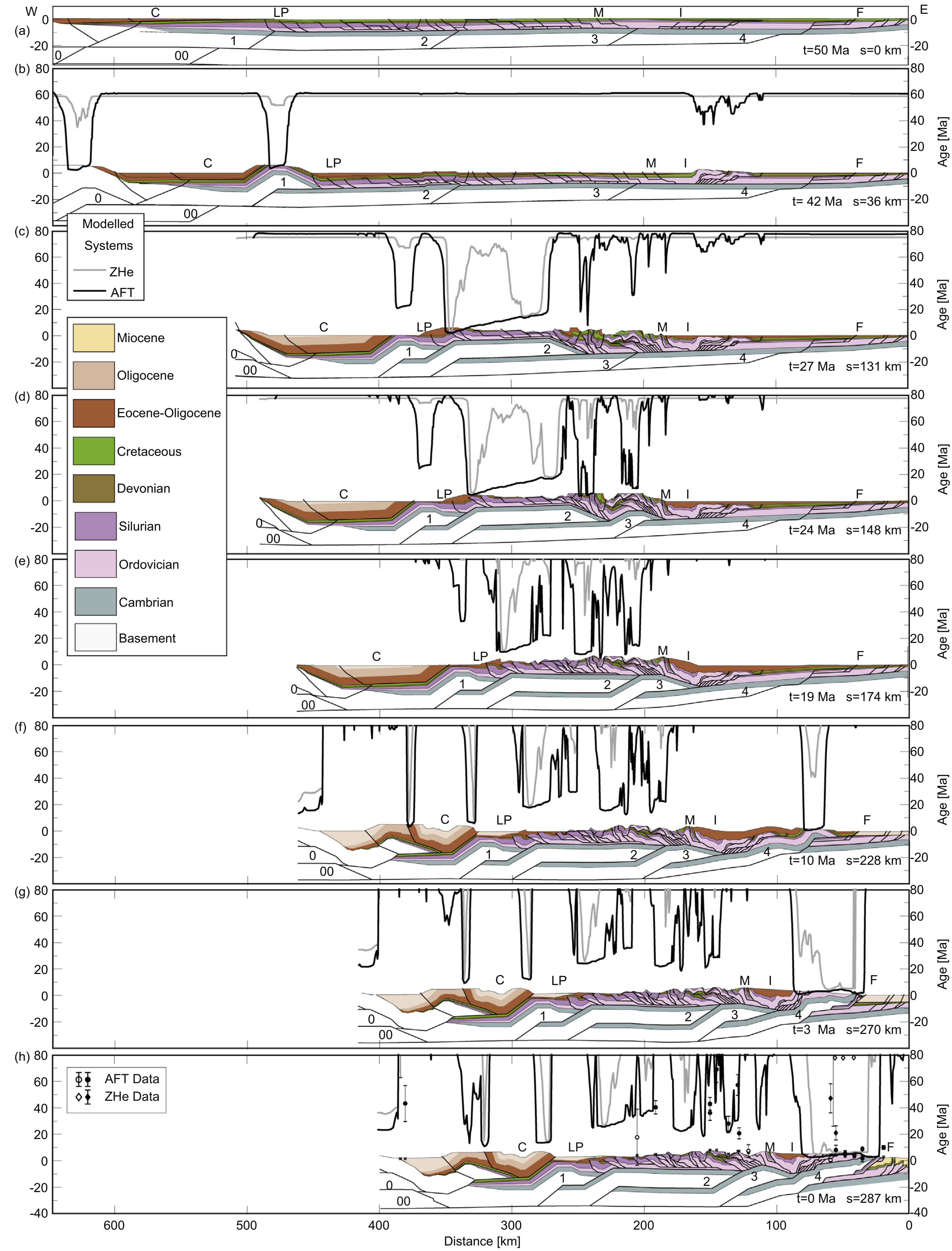

(caption on next page)

Fig. 5. Structural and thermochronologic evolution sequence in the central Bolivian FTB using model (1) kinematics and constant velocity. The (a) restored cross-section is (b)-(h) sequentially deformed with the top panel displaying the modelled thermochronology (AFT & ZHe) and the bottom panel showing the geometry of the deformed model. (h) circles indicate AFT samples, diamonds indicate ZHe samples (Table 1). Sedimentary basins: Corque (C), Lago Poopo (LP), Morochata (M), Incapampa (I), Foreland (F).

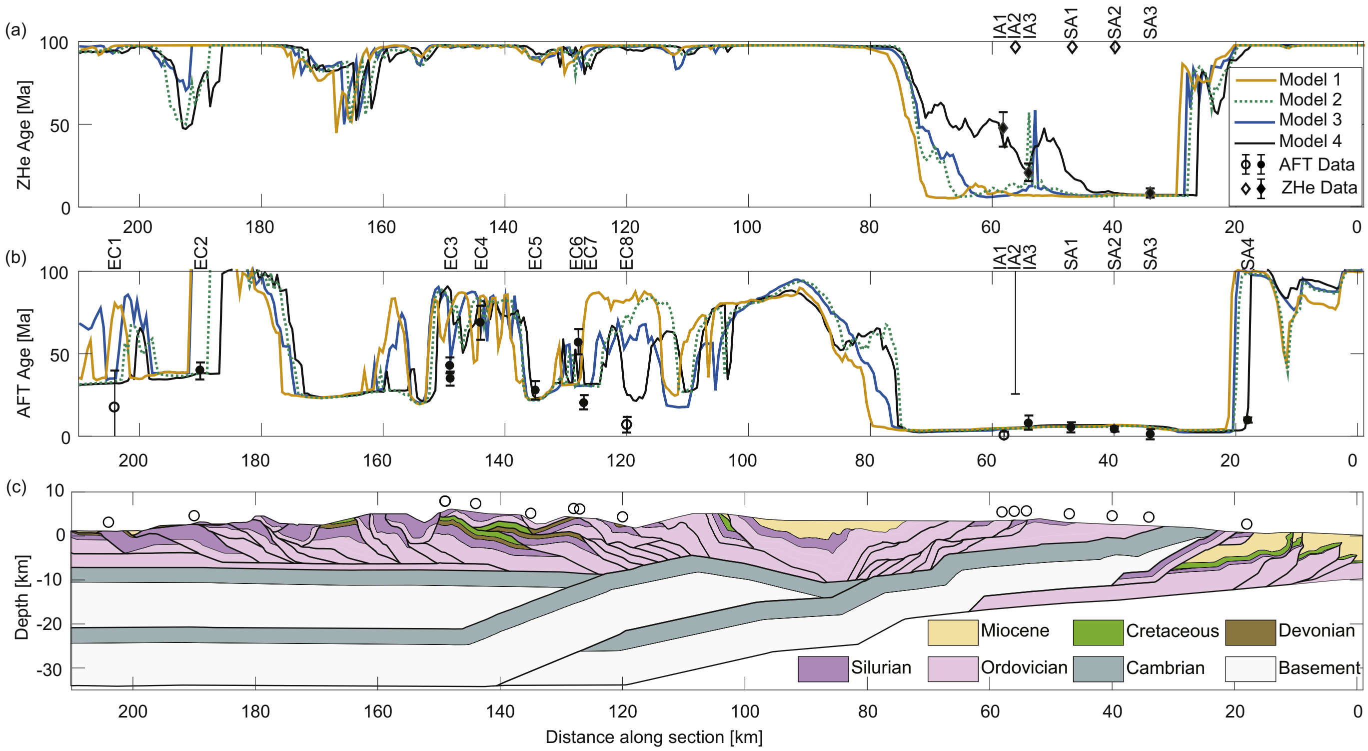

Fig. 6. Effect of Kinematics on thermal modelled ages; thermal structure and velocity are the same between models. (a) ZHe modelled and measured ages; open diamonds indicate locations of samples with mixed/partial reset ages, (b) AFT modelled and measured ages; open markers indicate samples with poor data resolution, (c) cross-section with no vertical exaggeration. Open circles indicate sample locations.

basement ramp, with narrower wavelength patterns set by previous shortening and exhumation focused in Paleozoic age rocks. This creates a mix of fully (~10 Ma) and partially reset AFT (~40 Ma) and ZHe (~50–70 Ma) ages at t = 4 Ma (Fig. 5d, 200–220 km). Exhumation induced by westward-propagating deformation in Paleozoic rocks above the hanging wall of basement thrust 2 predicts a reset AFT signal and partially reset ZHe signal between 240 and 250 km (Fig. 5d). The predicted ZHe and AFT signals between 250 and 310 km experience no additional exhumation and thus age with model time.

At t = 19 Ma (Fig. 5e), the predicted AFT signal due to exhumation induced by the emplacement of basement thrust sheet 1 is dampened by onlapping sedimentation in the AP (320–330 km, Fig. 5e). Shortening in the westernmost EC drives erosional exhumation of ~3 km of synorogenic sediments and the model predicts partially reset (~40 Ma) AFT ages at 315–320 km (Fig. 5e). Westward-propagating shortening in the Paleozoic cover overprints and narrows the signal from the emplacement of basement thrust sheet 2, resulting in a mix of partially reset (~50–60 Ma) and fully reset (~10–20 Ma) AFT ages between 310 and 260 km (Fig. 5e). This westward-propagation displaces the thin-skinned cover to the west, shifting the signal of ages reset due to emplacement of basement thrust sheet 3 to the west. The final emplacement of basement thrust sheet 3 drives exhumation in the previously deformed overlying Paleozoic cover between 200 and 250 km, predicting younger populations of partially (~35–40 Ma) and mostly unreset (~70 Ma) AFT ages (Fig. 5e). The ZHe signal across the entire section remains unchanged, as deformation in this step is insufficient to drive exhumation deep enough to expose rocks with reset ZHe ages.

At t = 10 Ma (Fig. 5f), modelled shortening in AP, first on the east and then west side of the Corque syncline, drives erosion and exhumes reset AFT and ZHe ages (385–375 and 330–320 km, respectively). Deformation in the EC has ceased, and thus the modelled thermochronology signal present in the EC in Fig. 5e is increasing in age. At t = 10 Ma, emplacement of basement thrust 4 has been ongoing for ~4 Myr, and uplift over the SA ramp at ~70 km exhumes reset AFT ages between 60 and 80 km, with the youngest ages (~0.5 Ma) at the ramp at ~80 km, increasing gently in age to ~4 Ma at 60 km (Fig. 5f). The predicted ZHe signal is partially reset to 40 Ma in the center of the U-shaped AFT pattern where the erosion level is the deepest at ~70 km (Fig. 5f).

At t = 3 Ma (Fig. 5g), continued emplacement of basement thrust sheet 4 over ramps in basement (~100 km), Paleozoic (~80 km), and Tertiary (~40 km) strata exhumes the reset AFT signal between 90 and 38 km. The AFT signal is reset between 90 and ~45 km due to the ramp through Cambrian and Ordovician rocks at 90 km in a westward-younging U-shaped pattern, with the youngest ages (~0.5 Ma) increasing gently to ~3 Ma at ~45 km (Fig. 5g). The easternmost SA ramp, located at ~40 km, reset AFT to ~0.5 Ma at 30–40 km. The ZHe signal is reset between 90 and ~45 km due to deformation over the SA ramp at ~90 km inducing the deepest exhumation levels in the Paleozoic strata (Fig. 5g). The break between predicted fully reset (~0.5 Ma) and unreset (> 80 Ma) ages is pinned at 30 km by the surface breaking fault.

At t = 0 Ma (Fig. 5h), the final 17 km of shortening in the SA brings thrust sheet 3 up and over the active basement ramp at ~120 km, which drives additional exhumation in the Paleozoic cover, resetting the AFT signal to ~20 Ma at 100–110 km (Fig. 5h). Shortening in the SA and continued emplacement of thrust sheet 4 exhumes the fully reset ZHe signal between 50 and 75 km to ~3–6 Ma (Fig. 5h). The final SA shortening, within the Tertiary foreland basin, does not produce enough exhumation to expose reset ZHe ages, and only exhumes partially reset AFT ages at ~14 km to ~42 Ma because of limited displacement on individual faults (Fig. 5h).

4.2.2. Kinematic variation and modelled thermochronology ages

We evaluated the effect of in-sequence and out-of-sequence (OOS) faulting on the predicted ages in the SA and IAZ by testing four different kinematic models, while holding velocity and radiogenic heat production constant. All models have IAZ and SAZ deformation from 10.4 to 0 Ma (Fig. 6). Model 1 has all of the SA and IAZ faults deform in-sequence, propagating from west to east, while models 2–4 have OOS motion as shown in Fig. 4.

4.2.2.1. Subandes and Interandes. At the front of the Subandean belt where the structures deform foreland basin deposits, all 4 models show partially reset AFT ages (~3–12 km from the deformation front, Fig. 6b). Exhumation is largely focused over the fourth SA fault (at 12 km) with predicted ages as young as 45 Ma, with less exhumation and older ages (80–90 Ma) over the second and third SA faults (2.5 and 9.5 km, respectively). In-sequence deformation (Model 1) predicts the youngest ages in this region, with similar ages predicted by Model 2 which has limited (3 km) of OOS motion. The larger amount of OOS motion in Models 3 and 4 post-date all but 1.9 km of motion on the frontal faults. The shift from active exhumation to subsidence in front of the OOS fault depresses the predicted AFT ages. At 19 km from the deformation front in Model 4 and 22 km in Models 1–3, the AFT signal shifts from unreset (~100 Ma) to fully reset (~0.5 Ma). These young predicted AFT ages extend to ~75–80 km from the deformation front (Fig. 6). The westward shift in the location of partially to fully reset ages, at 19 km for model 4 and 22 km for models 1–3, is controlled by both the amount of OOS motion and the specific SA/IAZ boundary fault that is last active. Model 4 has 15 km of OOS motion, with the final motion of OOS on the fault that breaks the surface 20 km from the deformation front. This amount of deformation and accompanying erosion exposes fully reset AFT cooling age behind the fault, such that sample SA4 is in front of the fault on the transition to unreset AFT ages. Models 1–3 have this transition from unreset to fully reset near ~22 km because of no additional OOS motion on the fault at 20 km.

The modelled ZHe signal is completely unreset in the frontal ~20 km of the cross-section but exhibits partially reset ages ~55–80 Ma (Fig. 6a) over the proposed OOS fault. Model 4, with the largest and youngest component of OOS motion produces the youngest modelled cooling ages in this region. All four models predict young reset cooling ages of 8 Ma at ~30 km from the deformation front. The predicted ZHe ages are fully reset (~8–10 Ma) until ~45 km (Model 4), ~63 km (Model 3), ~66 km (Model 2), and 70 km (Model 1), where the predicted cooling ages increase to significantly older ages, with the exception of narrow excursions of partially reset ~55 Ma ages at 55 and 53 km (for Models 2 and 3). Model 4 produces a more complicated predicted pattern of cooling ages with younger ~20 Ma ages at ~55 km before predicted ages continue to irregularly increase to ~55 Ma at 70 km from the deformation front.

Though all four kinematic models result in the same surface geology and erosion level in the end, the paths and erosion level through time are different (Fig. 4). This is particularly important for capturing the ZHe signal for samples IA1 and IA3. All four models are uplifted over ramps located at ~80, ~63, and ~30 km from the deformation front during SAZ deformation but the kinematic order controls which ramp is active when. Model 1 (in-sequence) predicts a smooth, fully reset ZHe signal set by the most recent shortening occurring only on the ramp at ~80 km, while Models 2 and 3 have a more complicated ZHe pattern imparted by recent exhumation over the ramp at ~62 km during OOS faulting (Fig. 6). The kinematics of Model 4, specifically no motion on the fault that repeats the upper Ordovician and Silurian strata, limits erosion early on in the sequence (Fig. 4 (iv) c), with final uplift towards the end of the model in a combination that allows the modelled ZHe ages corresponding to samples IA1 and IA3 to rest in the partial retention zone resulting is a suite of mixed and partial reset ages. While each kinematic model produces a different pattern of predicted ZHe ages from 35 to 75 km, the strong uplift signal over the ramp at from 30 to 40 km reproduces the young 8 Ma ZHe age of sample SA3 at ~33 km in all four kinematic models. The predicted ZHe ages to the west (35–75 km) are unique, allowing us use to samples IA1 and IA3, located 58 and 52 km from the deformation front, respectively, to differentiate between the viability of the kinematic models (Fig. 6a). From 70 to 80 km from the deformation front (Fig. 6), the modelled AFT signal highlights the effect of varying the most recent active ramp locations (bolded lines, Fig. 4 (i-iv) d). Model 1, which has in-sequence SA motion only, has the predicted young AFT signal pinned to near 80 km because this signal is driven by motion over the most recent ramp, which for Model 1 is located at ~80 km. However, Models 2–4 predict the young AFT signal near 75 km (Fig. 6); this is because these models have OOS motion that continues up the SA ramp near 62 km, which overprints the signal from the ramp at ~80 km. Model 4 best captures the ZHe signals in samples IA1-SA3 (Fig. 6a), and is the only kinematic model to accurately represent AFT sample SA4.

4.2.2.2. Eastern Cordillera. For all four of the proposed kinematic variations, the deformation in the EC is exactly the same, yet the predicted cooling ages in the EC have subtle variations due to different kinematics of IAZ and SAZ deformation that postdate deformation and exhumation in the EC. The EC has a low total amount of exhumation, making it particularly sensitive to small variations in erosion. This is highlighted by modelled ZHe ages that are never fully reset and only show slight resetting at 160–170 and ~190 km along the cross-section line. The youngest predicted ZHe ages are at 230 km, directly above the footwall ramp of basement thrust 3 (Fig. 5h; Fig. 6a). Individual faults that displace Paleozoic strata in the EC have small magnitudes of displacement and thus the primary exhumation is imparted by motion of basement structures and the associated erosion as illustrated in Fig. 5.

Modelled reset EC AFT ages are concentrated in 3 bands from ~110–135, ~150–175, and ~190–230 km (Fig. 6). The final modelled cooling ages in the eastern portion of the EC are a function of two periods of exhumation: initially as partially reset ages due to deformation-induced exhumation from shortening of the Paleozoic section (Fig. 5c, 240–250 km), and then exhumed further with the emplacement of basement thrust sheet 3 (Fig. 5d, e, 200–215 km). The central band of predicted reset ages was exhumed as west-vergent thrusting in Paleozoic rocks allowed for thrust propagation over the hanging wall ramp of basement thrust sheet 2 driving erosional exhumation (Fig. 5d, e). The western most band was exhumed and cooled due to the motion of basement thrust sheet 2 over its footwall ramp concentrating the youngest reset AFT ages in this region. Because of this shared history, there are only minor differences in the predicted cooling ages between the 4 different kinematic models in the two western most populations of reset AFT ages in the EC. Larger variations in the predicted ages from the four different kinematic models are present in the eastern population of reset ages between 110 and 135 km from the deformation front. This region is located at the edge of the critical wedge of increasing topography in response to uplift of basement thrust sheet 4 and SA shortening, and the timing of erosion is controlled by the timing of propagation of the deformation front. The deformation front of Model 1 (in-sequence) propagates forward slower than that of Model 4, resulting in older ages (Model 1: ~80 Ma vs Model 4: ~20 Ma) due to exhumation earlier in Model 1 between 110 and 135 km (Fig. 4, Supplementary Fig. 1). The amount of OOS motion, and on which fault, the pattern of modelled AFT ages in the EC between 110 and 135 km. Specifically, SAZ OOS motion affects the age of the partially reset AFT system, and where that resetting occurs, due to the region's sensitivity to variation in deformation front propagation and differences in loading associated with different kinematics. Modelled ZHe is unreset, or nearly unreset at > 90 Ma, in all kinematic models across the entire EC (80–210 km).

Two regions have particularly limited exhumation: 80–100 km, where foreland basin sedimentary rocks are preserved, and 135–150 km, where there is preservation of nearly the full thickness of a Paleozoic thrust sheet. The sedimentary layers accumulated in a foredeep/wedgetop position of the growing FTB (160–180 km, Fig. 5b-d), that experienced maximum subsidence during motion and loading from basement thrust 2 as well as initial loading from basement thrust 3. The partially reset AFT (40–80 Ma) ages at ~80–110 km (Fig. 6) are due to both the preservation of sedimentation as well as lack of exhumation as the basin is never fully exhumed over basement thrust sheet 3 (160–180 km, Fig. 5e), nor is the uplift over basement thrust sheet 4 enough to exhume the full thickness of synorogenic sediments (80–110 km, Fig. 5g). The basin preserved at 80–100 km in our model is not present at 18°S, however, similar basins preserving the Cretaceous through Tertiary sedimentary section exist further south (e.g., the Incapampa basin). Similarly, between 135 and 150 km, the clusters of partially reset ages (~60–80 Ma) were located in a region of low exhumation between basement thrust 2 and basement thrust 3 (Fig. 5d) and was never displaced over the footwall ramp of basement thrust 3 (Fig. 5d, 210–225 km) limiting exhumation. Additionally, these structures deformed early on in the EC backthrust sequence, and thus never had synorogenic sedimentation from Andean deformation deposited on top. This combination of lack of burial and lack of exhumation preserves nearly two full thicknesses of Paleozoic strata and leads to the cluster of partially reset ages (~60–80 Ma) between 135 and 150 km (Fig. 6).

The model-predicted EC AFT signal has multiple broad wavelength patterns primarily controlled by the emplacement and eastward propagation of basement thrust sheets, as illustrated in Fig. 5h and Fig. 6. This signal is augmented by smaller wavelength patterns that are a function of individual thrusts in the Paleozoic section. However, due to the lower overall amount of exhumation, this signal is overprinted by time since exhumation. As Model 4 is best able to capture the ZHe measured ages in the SAZ and IAZ and is equally good at capturing the AFT ages throughout the model space, we use kinematic Model 4 in subsequent sections.

4.2.3. Effect of Radiogenic Heat Production on modelled thermochronology

The effect of radiogenic heat production on the predicted cooling ages was evaluated using kinematic Model 4, and by modelling two different estimates of how heat production changes with depth; the first has a constant radiogenic heat production (A_o = 0.6–1.0 μW/m^3) through the entire crustal section, while the second applies a radiogenic heat production (A_o = 3.0–4.0 μW/m^3) that decreases exponentially with depth (e-folding depths of 12 or 15 km). Measured A_o values in the lower crust are difficult to obtain, and variation with in the lower crust is not negligible (Ashwal et al., 1987; Jaupart and Mareschal, 2011; Ketcham, 1996). In the Andes, surface heat flow measurements change significantly from the foreland (~35–60 mW/m^2) to the AP (70–140 mW/m^2), with an average surface heat flow across the FTB between 60 and 80 mW/m^2 (Ehlers, 2005; Henry and Pollack, 1988; Jaupart and Mareschal, 2011; Mareschal and Jaupart, 2013). Previous studies have found that surface heat flow modelled by a constant A_o applied to the entire crust (A_o = 0.9 μW/m^3) or an exponentially decaying A_o (A_o = 3.0 μW/m^3, ef = 0 km) produce nearly identical surface heat flow of ~56 mW/m^2 (Springer, 1999). Similarly, thermal models that use an e-folding depth require a higher heat production value to produce the same modelled ages as a thermal model that applies a constant heat production value to the entire crust (Fig. 7). Increasing A_o or e-folding depth (ef) in the crust raises geothermal gradients and results in younger modelled thermochronometer ages.

The modelled AFT pattern is most sensitive to changes in heat production in the EC (70–210 km, Fig. 7b), while ZHe is most sensitive in the IAZ and SA (18–70 km). With the highest heat production (A_o = 1.0 μW/m^3) the AFT signal becomes fully reset (17–30 Ma) across the entire EC, except for 90–100 km due to basin preservation and 135–150 km due to the kinematics discussed in Section 4.2.2. (Fig. 7b). Decreasing the heat production in the crust reduces the width of the cooling signal imparted by the basement thrust sheets, and instead allows visualization of the effect smaller scale structures have on cooling ages. Changes in heat production have the largest effect on the predicted cooling ages where the magnitude of exhumation is the least, such as between 70 and 160 km. Model-predicted ages become older with lower heat production as well as more variable (e.g. between 150 and 100 km, Fig. 7b). The cooling ages are predominantly partially reset (~40–80 Ma), with small wavelength fully reset ages (20–30 Ma) over individual Paleozoic structures (Fig. 7b). This same effect on predicted cooling ages, where model-predicted ages become older with cooler heat production, is also present in models with an e-folding depth. The warmest of these models, A_o = 3.0 μW/m^3, ef = 15 km, produces a more variable pattern, containing more partially reset ages, than that of the hottest model (A_o = 1.0 μW/m^3). This warmest e-folding depth model similarly highlights exhumation on smaller scale structures in the Paleozoic rocks (like A_o = 0.6 μW/m^3), though with younger partially reset ages. Reducing the heat production by decreasing the e-folding depth by 3 km, from 15 to 12 km, with A_o = 3.0 μW/m^3, produces the same pattern of small-structure dependent AFT ages, but with the overall magnitude of ages shifted older by up to ~16 Ma (Fig. 7b). A comparable result is seen by decreasing A_o, from 3.5 to 3.0 μW/m^3, with the same ef = 12 km, where ages are less reset via cooler temperatures in the crust (Fig. 7). The coolest model without an e-folding depth, A_o = 0.6 μW/m^3, produces similar modelled AFT ages, in both pattern and magnitude, as the coolest model with an e-folding depth, A_o = 3.0 μW/m^3, ef = 12 km (Fig. 7b).

For the ZHe system, the warmest modelled heat production, A_o = 1.0 μW/m^3, fully resets the entire SA and IAZ predicted ages to ~7 Ma (Fig. 7a), analogous to the predicted age pattern of Model 1 with in-sequence kinematics (Fig. 6a). Decreasing the available heat in the crust produces increasingly older populations of partial reset ages in the IAZ and on the western edge of the SA (from 40 to 70 km). Decreasing the e-folding depth by 3 km, from 15 to 12 km, for the same A_o = 3.0 μW/m^3, produces similar patterns of ZHe ages, with the overall magnitude of ages shifted older by up to ~34 Ma (Fig. 7a). Similarly, decreasing A_o from 3.5 to 3.0 μW/m^3 with ef = 12 km increases the predicted ages to ~37 Ma, but retains the cooling age pattern prescribed by exhumation on individual structures.

As discussed in Section 4.2.1, modelled ages are primarily controlled by the emplacement of basement thrust sheets, while changing heat production changes the magnitude of the ages and to which cooling signal the predicted ages are the most sensitive. High heat production values (e.g. A_o = 1.0 μW/m^3) highlights the control that basement thrust sheets impart on the exhumation. As heat production values are reduced, second order features become amplified as only individual structures (1–5 km in width), that focus exhumation, predict reset ages, separated by narrow regions of partially reset ages.

Models with constant radiogenic heat production simplify the thermal regime by applying this input radiogenic heat value across the whole crustal column. However, as radiogenic minerals tend to be at higher concentrations in the upper crust than in the lower crust (Heier and Adams, 1965; Jaupart et al., 2016), it is reasonable to wonder if this simplification may affect cooling ages. Therefore, to test the effects of this variance in crustal thermal structure, we compare models of a constant heat production versus those that have an exponential decay from the surface radiogenic heat value. For modelled AFT ages at the surface, the difference between A_o = 0.6 μW/m^3 with no e-folding depth and is negligible for an individual AFT chronometer (compare dashed to the two lighter grays, Fig. 7b). Using an e-folding depth produces cooler A_o values with depth and thus the difference in the predicted ages using surface heat production values and an e-folding depth or a constant heat production value is seen in the ages of the

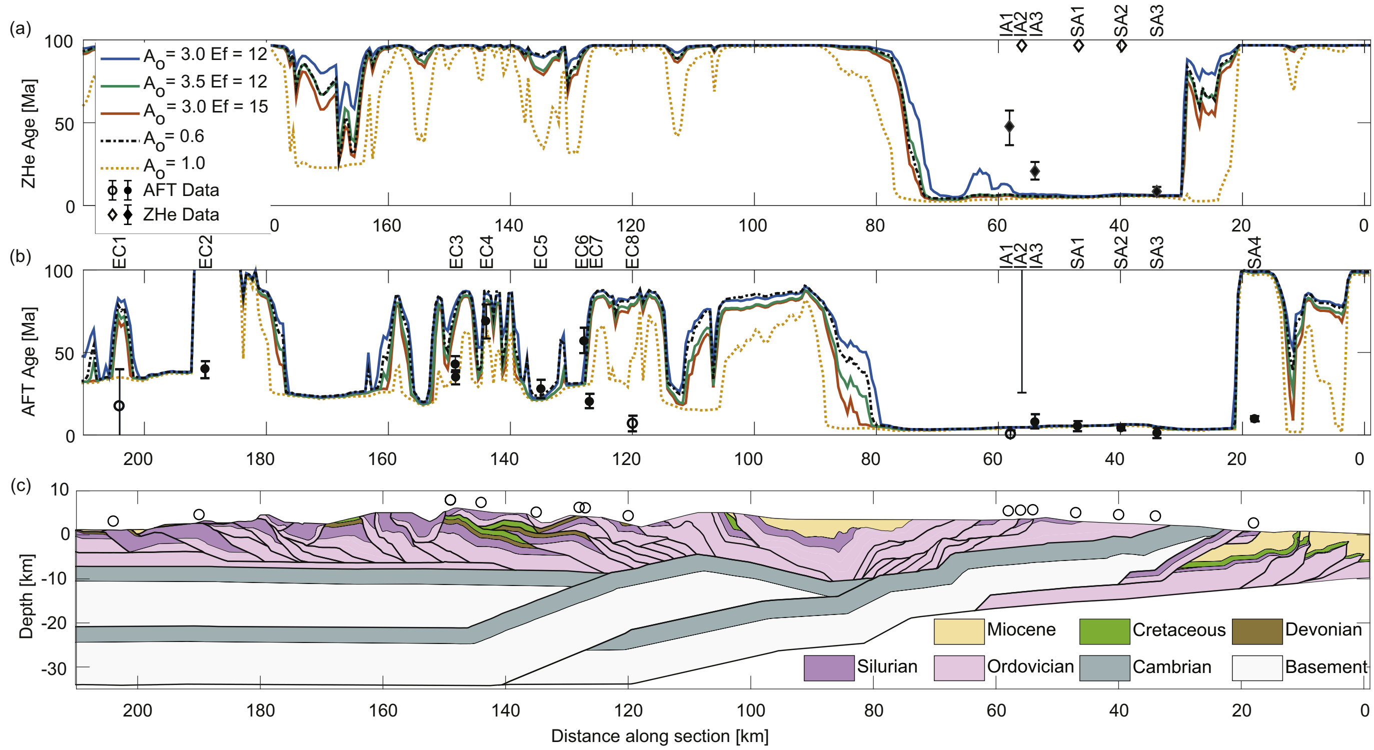

Fig. 7. Effect of Radiogenic heat production on thermal modelled ages for Model 4; kinematics and velocity are the same between thermal models. (a) ZHe modelled and measured ages; open diamonds indicate locations of samples with mixed/partial reset ages, (b) AFT modelled and measured ages; open markers indicate samples with poor data resolution, (c) cross-section with no vertical exaggeration. Open circles indicate sample locations.

deeper chronometers like ZHe. In our model, this is reflected as a greater span in ages between the predicted AFT and the predicted ZHe ages using an e-folding depth than at constant heat production values.

Cooler crustal temperatures can be produced by decreasing the e-folding depth or lowering $A_{o.}$ This lower heat predicts older AFT and ZHe ages, which better capture AFT sample EC6 and ZHe samples IA1 and IA3. Additionally, at depth, the temperatures achieved with $A_o = 0.6\,\mu W/m^3$ and no e-folding depth are unrealistic for crustal temperatures. For example, the crustal temperatures for $A_o = 0.6\,\mu W/m^3$ is ~720 °C at 40 km depth under AP, while with an e-folding depth of 12 km and $A_o = 3.5\,\mu W/m^3$, the crust is only ~533 °C (nearly 200 °C cooler).

Some portions of the model are, to a first-order, insensitive to the small changes we evaluated in how heat in the crust is distributed; the modelled AFT ages do not change in the SA (between 20 and 70 km), or in the western half of the EC (150–220 km). AFT samples EC1, EC2, EC5, and all IAZ and SA samples do not differentiate between heat production values. Both EC3 AFT samples are only predicted by the warmest heat production values ($A_o = 0.6\,\mu W/m^3$, and $A_o = 3.5\,\mu W/m^3$, ef = 12 km within error). Only the coolest AFT models match EC6 ($A_o = 3.0\,\mu W/m^3$, ef = 12 km; $A_o = 0.6\,\mu W/m^3$), while none of the models are warm enough to predict ages that match EC8, though this may be due to an anomalously young measured age. The AFT measured ages, while not a strong distinction, are best fit by models with cooler heat production.

Modelled ZHe ages are unaffected in the frontal portion of the SA between 30 and 40 km (Fig. 7). Because much of the EC has not exhumed enough to reset ZHe ages, these predicted ages are also insensitive to changes in heat production. However, from 40 to 70 km, the ZHe modelled ages are responsive enough to changes in radiogenic heat production that with increased heat production the sensitivity to the kinematics (Fig. 6) is removed. ZHe sample SA3 does not distinguish between heat production, but samples IA1 and IA3 are only predicted in the coolest heat production values ($A_o = 3.0\,\mu W/m^3$, ef = 12 km and $A_o = 3.5\,\mu W/m^3$, ef = 12 km, respectively). Predicted AFT and ZHe modelled ages provide the best fit to measured thermochronology samples when using a thermal heat production slightly warmer than the lowest shown in Fig. 7; therefore, $A_o = 3.2$ and an e-folding depth of 12 km is used in subsequent sections.

4.2.4. *Effect of shortening rate on modelled ages*

We evaluated the effect of changing shortening rate on model-predicted thermochronology ages by analyzing a suite of velocity models, including constant velocity (*i*, ~5.8 mm/yr), SA fast deformation (*iii*, *vi-ix*: 6–10 mm/yr), a hiatus in EC deformation during 40–20 Ma (*ii*, ~4 mm/y), and variations on a rapid pulse of deformation (*iv*: 11.5 mm/yr, 6–2 Ma; *ii*, *x*: 8–12 mm/yr, 16–6 Ma; *v*: 10 mm/yr, 11–5 Ma, 4 mm/yr 5–0 Ma) on kinematic model 4 (Fig. 8a, Table 4, Supplementary Fig. 2).The most important result is that velocity changes do not significantly alter the across-strike cooling pattern, as that is controlled by kinematics. Instead, velocity changes can shift the ages older or younger, broaden the suite of reset ages, flatten the slope of ages, and reduce (or amplify) the appearance of second-order patterns in cooling ages. In this section, we present three velocity frameworks to show the effect of shortening rate on modelled ages. The simplest velocity framework, constant deformation through all Andean deformation, is here compared to two variable velocity frameworks to test their effects on modelled ages, particularly during SA deformation. All three velocity frameworks shown in Fig. 9 have the same initial deformation rate, ~5.8 mm/yr, at model start time. However, they differ in the shortening rate during SA deformation. Velocity *i* remains at a constant ~5.8 mm/yr during the entire SA deformation, which begins at ~10 Ma. Velocity *v* has an initial rapid (10 mm/yr) pulse of SA deformation from ~12 to ~10 Ma, and then decreases to 4 mm/yr from ~10 Ma till present. Velocity *viii* has a ~10 mm/yr shortening rate during the entire SA emplacement, which begins at ~6 Ma (Fig. 9).

4.2.4.1. Subandes and Interandes. At the front of the SA, all velocity

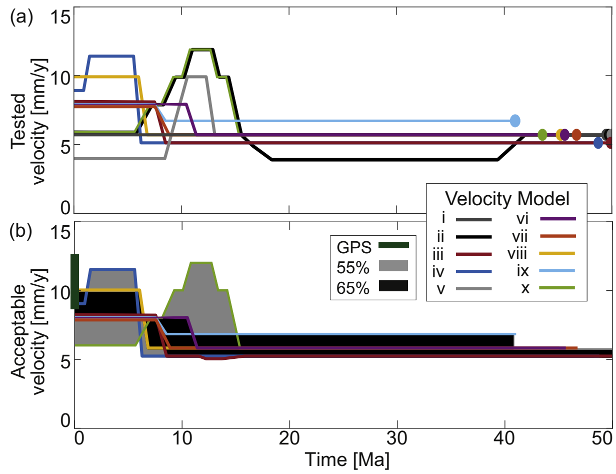

Fig. 8. Shortening rate versus time showing (a) suite of velocity models tested (corresponding to Table 4); closed dots indicate model start time. (b) acceptable velocity envelope for kinematic Model 4 defined by thermochronologic age match of > 55% (gray) and > 65% (black); green bar is modern GPS shortening rate.

Table 4
Summary of velocities modelled, SA velocities and ages, and percentage fit. **Bold** is age of SA initiation. Modelled thermochronology error is ± 1 Ma and ± 2 km along section. Percent Fit is computed by number of measured samples that fall within the model error divided by the total number of measured samples. Note: the first ~11.4 km of SA shortening is interfingered with the last 11.5 km of AP shortening. The * full rate given in column is partitioned between AP and SA shortening.

Velocity framework		SA rate		Percent fit	
		AP + SA	SA	Model 1	Model 4
50 Ma start					
i	All @ 5.8 mm/y (“Constant”) *	1.8–4.6 mm/y **14.48**–11.81 Ma	5.78 mm/yr 11.81–0 Ma	52.38%	47.62%
ii	Hiatus 40–20 Ma, SA + AP @ 10–12 mm/yr *, SA 6–10 mm/y	3.8–8.0 mm/yr **11.53**–10.12 Ma	6–10 mm/yr 10.12–0 Ma	47.62%	52.38%
iii	SA @ 8 mm/y *	1.65–4.2 mm/yr **11.52**–8.54 Ma	8 mm/yr 8.54–0 Ma	57.14%	71.43%
iv	6–2 Ma @ 11.5 mm/yr, 2–0 Ma @ 9 mm/yr *	1.65–4.2 mm/yr **9.24**–6.26 Ma	9–11.5 mm/yr 6.26–0 Ma	52.38%	61.90%
v	11–5 Ma @ 10 mm/yr, 5–0 Ma @ 4 mm/y *	1.8–4.6 mm/y **15.79**–13.11 Ma	4–10 mm/yr 13.11–0 Ma	42.86%	52.38%
45 Ma start					
vi	SA + AP @ 8 mm/y *	2.4–6.4 mm/yr **10.22**–8.54 Ma	8 mm/yr 8.54–0 Ma	47.62%	71.43%
vii	SA @ 8 mm/y *	1.8–4.6 mm/y **11.21**–8.54 Ma	8 mm/yr 8.54–0 Ma	57.14%	71.43%
viii	SA @ 10 mm/y *	1.8–4.6 mm/y **9.51**–6.83 Ma	10 mm/yr 6.83–0 Ma	52.38%	71.43%
40 Ma start					
ix	SA@ 8 mm/y *	2.16–5.44 mm/yr **10.81**–8.54 Ma	8 mm/yr 8.54–0 Ma	57.14%	71.43%
x	SA + AP @ 10–12 mm/yr, SA 6–10 mm/y *	3.8–8.0 mm/yr **11.53**–10.12 Ma	6–10 mm/yr 10.12–0 Ma	57.14%	61.90%

frameworks shown exhibit partially reset AFT ages (~75–87 Ma) due to deformation-induced exhumation consistent with Model 4 (Fig. 9b, ~3–12 km). Both velocity frameworks with slow SA deformation, velocities *i* and *v*, show slightly younger partially reset ages across this region (~75–92 Ma, ~3–12 km) than the fast SA velocity model (*viii*) (~88–95 Ma). Between 20 and 75 km, all velocity frameworks produce fully reset AFT ages, with the youngest reset ages (2–4 Ma) corresponding to the fastest SA emplacement (velocity *viii*), and the oldest reset ages (~5–12 Ma) corresponding to the slowest SA emplacement (velocity *v*). Faster rates during entire SA deformation young the AFT cooling ages, both because the timing of deformation is younger and faster rates produce flatter cooling curves (Fig. 9.

Predicted ZHe ages are all partially reset from ~18–26 km. Slower velocities *i* and *v* (~32–73 Ma) predict ages up to 32 Myr younger than those of the fastest velocity *viii* (~64–90 Ma) because the faster rate on the OOS fault dampens the predicted age pattern (i.e. restricts exhumation) in front of it (~20 km) (Fig. 9a). Predicted ZHe ages are completely reset west of the OOS fault at ~22 km in all frameworks. Cooling ages range from ~6 Ma (*viii*) to ~10–14 Ma (*i* and *v*). Between 33 and 75 km, model *i* predicts increasingly older ZHe partially reset ages (~75–90 Ma), while velocities *v* and *viii* remain completely reset until ~42 km, where predicted ages show a more complicated partially reset age pattern (~15–55 Ma) that has a zone of younger partially reset ages between 50 and 60 km.

Velocities *v* and *viii* have a nearly identical pattern of predicted ages between ~25 and ~70 km, offset by ~6 Myr, that do not overlap in time because the signal is set by initial SAZ fault motion at 10 mm/yr, regardless if that rate starts at ~7 Ma or at 13 Ma. These two frameworks have the exact same velocities during EC and AP emplacement, and differ only in velocity for the most recent ~42 km of shortening. This portion of the ZHe signal is collocated with samples IA1, IA3 and SA4, whose ages we argue are replicated in the signals of velocities *v* and *viii*, within error, but not in that of constant velocity *i*. Thus, the shape of the pattern of ZHe reset ages requires velocities greater than ~5.8 mm/yr (that of model *i*), and that, the timing of this fast emplacement of models *v* and *vii* within model error are equivalent, but that model *viii* is on the outer edge of this error envelope.

4.2.4.2. Eastern Cordillera. Across the EC, velocity frameworks *v* and *viii* have more fully reset AFT ages and younger partially reset ages than the constant velocity *i* particularly between 100 and 135 km; though the bulk of this pattern is controlled by kinematics, the faster velocities result in more fully reset ages by driving younger exhumation that occurs during SAZ deformation (particularly between 100 and 135 km, Supplementary Fig. 1). Velocity *viii* has EC ages ~3 Myr younger than those in *v*, as the duration of rapid shortening in the SA results in the timing of deformation in the EC being younger.

4.3. Best fit velocity models

Modelled thermochronologic ages predicted by various velocity structures for two kinematic variations (in-sequence, model 1, and OOS, model 4) were compared based on their ability to reproduce the measured thermochronology (AFT, ZHe) ages, all of which were given equal weight. Matches between measured and modelled ages were identified if the modelled age, with a ± 1 Ma and ± 2 km error, fell within any portion of the measured age and its error. The total percent fit is computed by dividing the number of matches by the total number of samples (Table 4, Supplemental Fig. 5). For constant velocity, Model 1 (in-sequence deformation) matches better (*i*, 52%) than Model 4 (*i*, 47%) (Table 4). However, for all other velocity frameworks, Model 4 consistently produces better results than Model 1, by 5–19%.

Sensitivity to model start times (50, 45, 40 Ma) was tested with the same SA velocity frameworks (8 mm/yr, ~8–0 Ma, Supplementary Fig. 3), but with three different rates during EC and AP deformation (5.2, 5.8, and 6.8 mm/yr). All three models match the thermochronology data equally well (71%, models *iii*, *vii*, *ix*; Table 4), though velocity *ix* lies on the outer edge of the error envelope (40 Ma start). This sensitivity to model start suggests that the EC is relatively insensitive to variation between ~5 and ~7 mm/yr deformation rates or

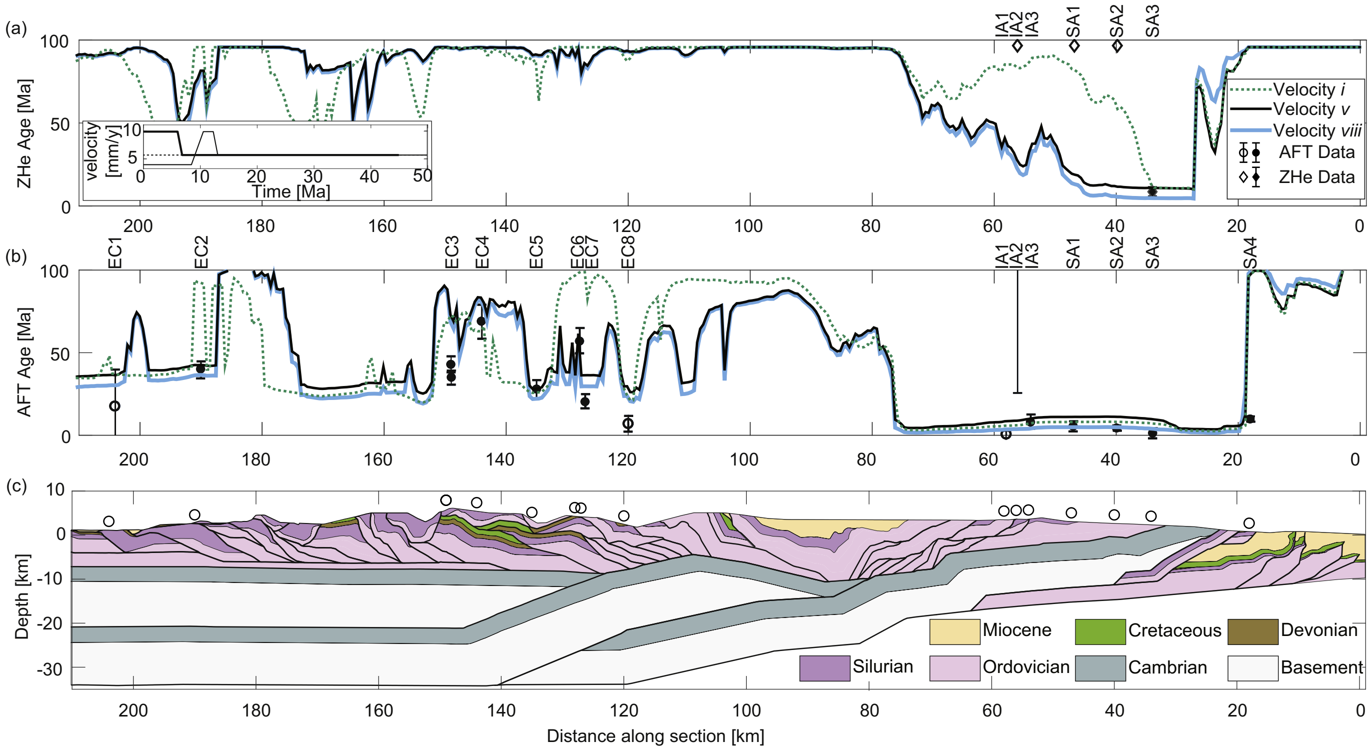

Fig. 9. Effect of velocity on thermal modelled ages; kinematics and thermal structure are the same between models. (a) ZHe modelled and measured ages; open diamonds indicate locations of samples with mixed/partial reset ages; inset with velocity structure; (b) AFT modelled and measured ages; open markers indicate samples with poor data resolution, (c) cross-section with no vertical exaggeration; open circles indicate sample locations.

age of initiation between 40 and 50 Ma, with a slightly better fit at > 5.2 mm/yr and model start > 40 Ma. Additionally, velocity *ii*, with EC deformation occurring at 4 mm/yr, has a lower percentage fit than velocity *x* whose EC deformation occurs at 5.7 mm/yr (52% vs 62%) and the 40 Ma start of deformation just barely captures the younger error limit for sample EC2. These observations highlight the critical velocity for EC thermochronologic fit as at least 5.2 mm/yr while the youngest permissible age of deformation is 40 Ma.

Velocity frameworks with greater than 55% fit for kinematic Model 4 were used to define an acceptable velocity envelope, shown in Fig. 8b. The best fit velocity frameworks (65% or greater match) require the SA to be 8–10 mm/yr (Table 4), and EC deformation at 5.2 mm/yr or greater. Five velocities result in the same percentage fit: *iii, vi, vii, viii,* and *ix* with a fit of 71.43%. As velocities *iii, vii,* and *ix* all have the same shortening rate during SA deformation (8 mm/yr) but different deformation (50, 45, 40 Ma) start times, we compare velocities *vi, vii,* and *viii* (all with a 45 Ma initiation of deformation) to remove any variation in modelled thermochronology due to variation in model start time. For ZHe sample IA2, velocity *vi* provides a better fit, rather than at the edge of the model error envelope (Fig. 10d). For ZHe sample SA3 and AFT samples IA3, SA1, SA2, and SA4, models *vi* and *vii* provide a better fit than *viii* (Fig. 10e-g). Model *viii* only provides a better fit than *vi* or *vii* for AFT samples IA1 and SA3 (Fig. 10f). As velocity *vi* best predicts the measured ages of the majority of SA thermochronology samples within a smaller error envelope than the other two velocities, velocity *vi* is used for modelled sedimentology ages in Fig. 11.

4.4. Modelled sedimentology

As flexural loading, due to the generation of new topography by crustal shortening in the kinematic model, is accounted for, the previous depositional horizon subsides creating a modelled stratigraphy. These flexurally-created foreland and hinterland basins initially form by deposition up to 0 km elevation. To continue sedimentation during and after deformation in the AP, sediment was accumulated in topographic lows up to 0.5 km per step. We compare the model-predicted age and thickness of stratigraphy in five distinct regions to their correlative published strata using our best-fit velocity model (Fig. 11). Model-associated ages are listed on the left, while the measured formations corresponding to thickness are listed on the right (Fig. 11 (a)–(e)).

4.4.1. Corque

Modelled synorogenic sedimentation in the Altiplano produced a westward thickening 1.1–3.2 km total of backbulge, forebulge, and foredeep sediments prior to thermal model initiation due to 200 km of shortening in the proto-WC FTB. These modelled strata may be correlative to the Santa Lucia, El Molino Fms, and basal Potoco (Fig. 2, Fig. 5a) depending on the start of EC deformation (early 50 Ma starts precludes the ~40 Ma base of the Potoco Formation as part of these early synorogenic strata). As modelled deformation in the EC begins, uplift over two basement ramps, one west and one east of the AP, provides a sediment source and loading mechanism for the AP. This shortening is transferred up these two basement ramps and into the Paleozoic section, which shortens initially eastward, and then propagates back west through the EC (Fig. 5b–e). The Corque syncline is situated between these two loci of deformation (e.g. basement ramps) and has ~4.5 km of modelled hinterland sediment accumulated by ~36 Ma, corresponding to the Eocene Lower Potoco, and ~4 km of modelled synorogenic sediment by ~28 Ma corresponding to the Oligocene Upper Potoco (Fig. 11a).

The modelled subsidence was restricted due to imposed isostatic uplift which slowed accumulation, resulting in only ~4 kms more of accumulated sediment by ~11.6 Ma (Fig. 5f), and ~2 km more by 0 Ma restricted to the topographic lows in the core of the syncline only, corresponding to the lower Miocene Coniri and upper Miocene to Quaternary upper Totora and Crucero Fms (Fig. 5h, Fig. 11a).

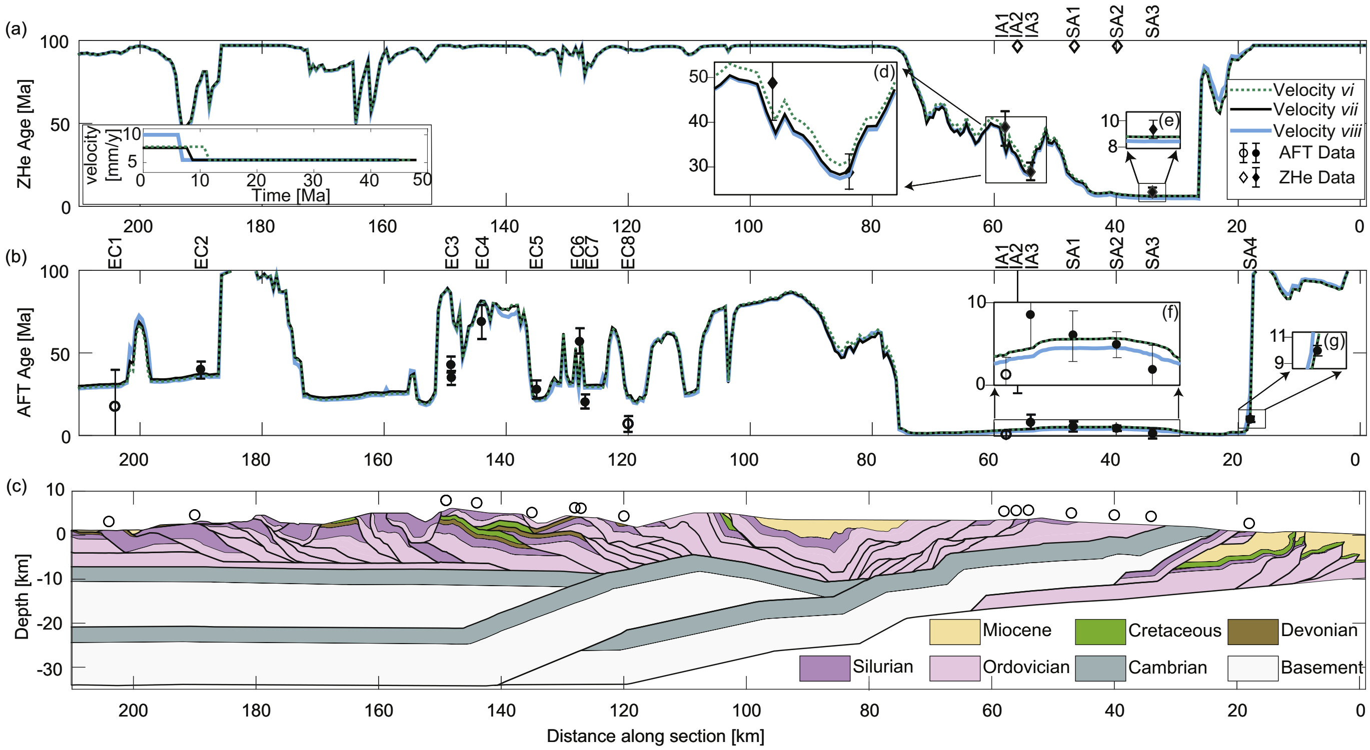

Fig. 10. Best fit velocities vi, vii, and viii. Insets (d)-(g) highlight important variations between the models and their abilities to fit SA thermochronology data. Kinematics and thermal structure are the same between models. (a) ZHe modelled and measured ages; open diamonds indicate locations of samples with mixed/partial reset ages; inset with velocity structure; (b) AFT modelled and measured ages; open markers indicate samples with poor data resolution, (c) cross-section with no vertical exaggeration; open circles indicate sample locations; (d) ZHe samples IA1 and IA3; (e) ZHe sample SA3; (f) AFT samples IA1 through SA3; (g) AFT sample SA4.

4.4.2. Lago Poopo

Lago Poopo modelled sedimentation initiated around ~25 Ma after OOS motion allowed erosional removal of up to ~6 km of synorogenic and the Cretaceous through Devonian overburden (Fig. 5d). Flexural-induced subsidence, due to shortening in the adjacent AP, allowed 4.8 km of synorogenic sediment accumulation between ~22 and 6.5 Ma (Fig. 5f), with 0.4 km more between 6.5 and 0 Ma (Fig. 11b). The restricted subsidence 6.5–0 Ma is primarily due to the locus of deformation, and thus subsidence, shifting ~170 km towards the foreland, with a secondary component due to imposed isostatic uplift.

4.4.3. Morochata

The 0.3 km of modelled backbulge sedimentation corresponding to the bulk of the Santa Lucia and El Molino Fms formed prior to the initiation of thermal modelling (Fig. 2, Fig. 5a). At the initiation of deformation, Morochata lies in a forebulge position (Fig. 5a). As deformation initiates in the modern FTB, Morochata lies between two loci of deformation, the eastward propagating deformation in Paleozoic rocks to the east and the basement ramp located to the west (Fig. 5b). As the isostatic response is dominated by the loading associated with the basement ramp, the remaining sedimentation occurs in the position

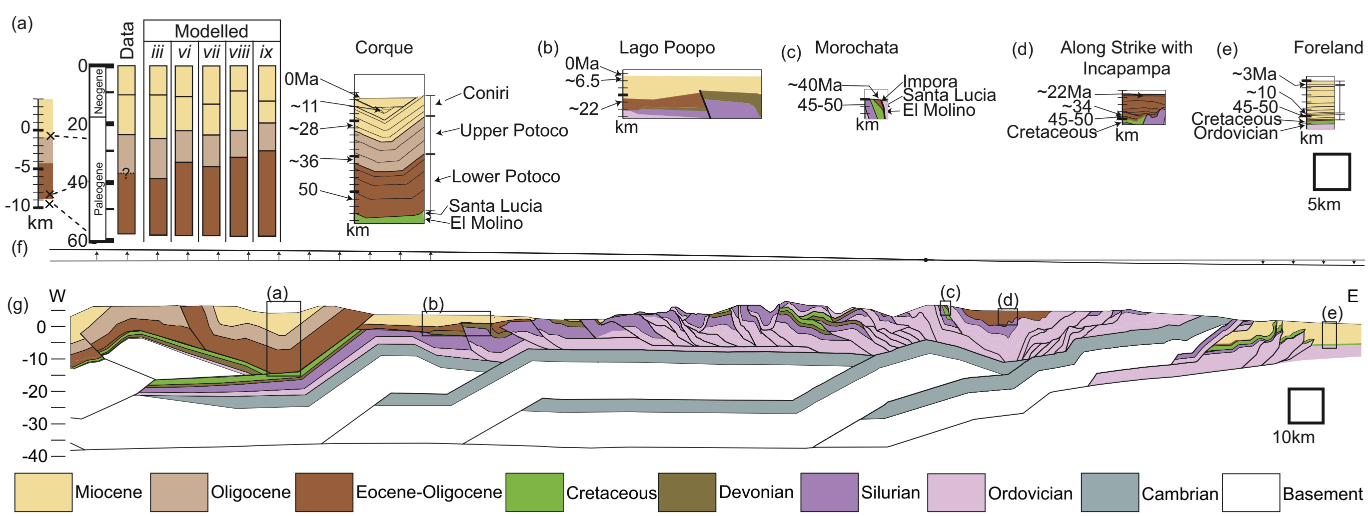

Fig. 11. (a)-(e) Sedimentary basins and associated model ages [Ma]; Ticks every kilometer for vertical scale; bold every five. (a) Variation in modelled sedimentology ages. (f) Schematic depiction of imposed uplift and subsidence showing locations of uplift and subsidence. (g) Final flexural-kinematic model showing (a)–(e) with no vertical exaggeration. Stratigraphy insets at 2× Cross-Section Scale.

of the foredeep/wedgetop, with 0.3 km forming by ~43 Ma and 0.2 km more by ~40 Ma (Fig. 11c).

4.4.4. Along strike with Incapampa

Although initial modelled deformation in the Paleozoic strata of the FTB starts on the eastern edge of the EC (Fig. 5b), as the basement thrusts propagate eastward and the overlying deformation propagates westward into the EC, the EC/IAZ boundary is a region of subsidence and basin formation (Fig. 5c, d). The modelled subsidence in the region is limited prior to ~34 Ma, as the loading is controlled by the emplacement of basement thrust sheets 1 and 2 and thus focused in the hinterland. This results in a very condensed section of sedimentation of only 0.1 km between 50 and 34 Ma (Fig. 5b). However, as the FTB grows and the décollement deepens in response to continued, eastward-propagating shortening of the basement thrust sheets, the eastern edge of the EC transitions to a more proximal foredeep location in front of basement thrust 3 and accumulates ~2.7 km of modelled synorogenic sediment by 22 Ma (Fig. 5d, e, Fig. 11d). No sediments are preserved after this time due to erosional removal from uplift and emplacement of basement thrust sheet 4 (Fig. 5g). As described in Section 4.2.2, our model preserves this sedimentary section that is not preserved in the FTB at 18°S due to insufficient exhumation over basement thrust sheets 3 and 4.

4.4.5. Foreland Basin

Modelled sediments in the foreland initially accumulate quite slow, with only ~0.35 km of sedimentation occurring between the model start and ~10 Ma due to the hinterland focus of shortening and weak initial lithosphere not forcing flexural subsidence far from the locus of deformation (Fig. 5a-e). As the deformation front propagates forward and shortening is focused in the IAZ and SA, the FB transition to proximal foredeep (Fig. 5f). The bulk of the FB sedimentation, the remaining ~4 km, occur between ~10 and 0 Ma due to flexural and imposed subsidence in the proximal foredeep of the FTB (Fig. 5f–h, Fig. 11e).

5. Discussion

5.1. Basement thrust sheet controls on kinematics, exhumation, and cooling signals

The pronounced changes in structural elevation between the SA, IAZ, and EC, in combination with the projected décollement depth, leaves a large space to be filled between the depth of the Paleozoic strata underneath the SA and its projection towards the hinterland and the exposed Paleozoic rocks at the surface in the IAZ and EC. These pronounced structural elevation changes have been interpreted as a function of basement thrust sheets in crustal scale cross-sections (Anderson et al., 2017; Baby et al., 1997; Kley, 1996; Kley et al., 1999; McQuarrie, 2002; McQuarrie et al., 2008a; Müller et al., 2002; Rak et al., 2017), although the geometry of the basement thrusts may differ. While duplexing of sedimentary rocks would fill the space, it would significantly increase the magnitude of shortening (McQuarrie, 2002), and require substantial removal of crustal rocks (Eichelberger et al., 2015). Provided there is an appropriate strength contrast between strong basement rocks and weak rocks due to the brittle-ductile transition, emplacement of a long basement thrust sheet requires less work than duplexing (Hatcher and Hooper, 1992; Mitra and Boyer, 1986). The initial cross-section geometry in this study (from McQuarrie, 2002) used three basement thrust sheets (with one very long thrust sheet) as a balance between the need for structural elevation and reduction in the amount of work necessary to deform. However, the initial geometry placed the hangingwall/footwall cutoff of basement thrust sheet 2 underneath a preserved thrust of Paleozoic through Cretaceous strata (near ~300 km in Fig. 5a). Basement thrust sheet 1 has ~33 km of displacement, and the majority of loading in the initial FTB is focused within ~50 km of this uplift (275–400 km, Fig. 5b). As displacement propagates forward and shortening begins on thrust sheet 2, the Cretaceous strata (preserved in modern times) are located near the surface (~0 km elevation) (~260–300 km, Fig. 5b). The initial basement thrust sheet 2 ramp was located directly below this and uplifted the previous topographic surface to > 10 km in elevation, regardless of EET tested. Any viable estimate of topographic elevation resulted in erosional removal of Cretaceous through the middle of Ordovician section. In order to preserve these Cretaceous through Ordovician strata present in the modern FTB, the basement thrust sheet was split into two and the ramp location was shifted to lie under the deepest erosion level with the majority of the cross-section remaining unchanged. Due to the strong relationship between basement thrust propagation and erosion, an obvious way to test the new basement geometry is to see if its predicted ages agree with measured ages though the region. The match between predicted and measured cooling ages as well as the flexurally produced basins all support basement thrusts as a viable method for transferring slip from deeper décollement levels up to the thin-skinned surface thrusting seen in the Central Andes. The incorporation of flexural modelling of basement thrust sheets imparted a new constraint to evaluating the viability of a cross-section and cross-section kinematics and highlights the large effect basement thrusts have on the location of exhumation.

Differences in the geometry and location of basement structures, as well as the proposed kinematics and vergence, should impart notably different mineral cooling ages. Baby et al. (1997) show two cross-sections through northern (15–18°S) and southern (21–22°S) Bolivia. Both sections show four to five eastward stepping basement thrusts similar to the four eastward stepping basement thrusts we propose for our section at 17–18°S. Notable differences include: 1) the thickness of these thrust sheets, the Baby et al. (1997) basement structures involve the entire thickness of the basement (20–25 km) compared to the ~12 km thrust sheets in the cross-sections we model, and 2) the location of the proposed modern, active ramp. The southern section of Baby et al. (1997) depicts a steep, active basement ramp located near the center of the EC. This steep basement ramp would produce a modern westward-younging signal similar to the signal basement thrust sheet 2 produced at ~24–27 Ma (Fig. 5c, d). The northern cross-section (15–18°S) has the active ramp even farther to the west. The young 0.5–8.1 Ma AFT ages between 20 and 60 km from the deformation front at 18°S (Fig. 10f, Table 1) requires that the active ramp at this latitude is located near the EC-IAZ boundary (Fig. 1).

Armijo et al. (2015) depict an orogen scale cross-section located at 21°S. In contrast to the eastward-verging basement structures proposed by Baby et al. (1997) and this study, the basement structures are predominantly west-verging (Armijo et al., 2015). The proposed westward-verging and westward-younging basement thrusts would provide uplift and exhumation in the eastern cordillera form 40 Ma to 10 Ma with the youngest ages (10 Ma) above the active ramp in the western EC. This kinematic scenario and timing are hard to reconcile with the measured thermochronology in the area (Anderson et al., 2018; Calle et al., 2018; Ege, 2004; Ege et al., 2007; Tawackoli, 1999). However, Armijo et al. (2015) additionally provide surface observations of west-vergent structures west of the WC that accommodate 10's of kilometers of shortening. These west-vergent structures are not incompatible with the predominantly east-verging WC basement ramps that facilitate 100's of kilometers of shortening in the EC, IAZ, and SA that we present here.

The focused uplift imparted by basement ramps produce locally high topography and an increase in erosional exhumation (Fig. 5). In our model, basement thrust sheets are the primary driver of uplift and exhumation, and thus impart the youngest ages above the active ramps (see Fig. 5c). Shortening over the hinterland footwall ramp due to emplacement of basement thrust sheet 2 produces the westward-younging AFT reset signal recorded by the two furthest west EC samples (180–250 km, Fig. 5h). Eastward propagation of this basement thrust sheet forms a crustal-scale, passive roof duplex which produces an eastward-younging cooling signal as westward propagation of the EC backthrust belt move material up and over the hangingwall ramp (Fig. 5d). These two patterns, when combined, have the oldest ages near the center of the EC (~160–150 km), bordered by westward-younging and eastward-younging patterns such that the youngest ages are on the outer edges of the EC (Fig. 5h). This pattern is slightly obfuscated by low exhumation (most notably at 180 km), where the pattern of basement faulting is only seen in the youngest reset ages (Fig. 5, Fig. 7), but can be augmented by increased heat production or velocity (Figs. 7 and 8). Low exhumation imparts a saw tooth pattern of reset and partially reset ages with a higher frequency (shorter wavelength) that highlights the exhumation induced by deformation on individual Paleozoic structures, complementing the broad wavelength cooling signal imposed by basement thrust sheets. We argue that this combination signal is recorded in our measured AFT ages where adjacent samples can have a difference in age of 25–30 Myr (e.g. samples EC3 and EC4), a range replicated between reset and partially reset ages in our model. Further eastward propagation of deformation emplaces the final basement thrust up and over its basement ramp and cuts through the full Paleozoic through Cenozoic section where it breaks the surface at ~20 km (Fig. 5h, Fig. 6b). This series of ramps produces a shallowly sloped westward-younging signal where the western edge is pinned at the ramp through the lower Paleozoic section (~75 km, Fig. 5g). Superimposed on this westward-younging signal are young ages that are a function of the OOS fault and the frontal ramp through the SA foreland basin. This combination of predicted signals matches the measured thermochronology.

5.2. Sedimentary Basin Formation

Sedimentary basins in retroarc systems encapsulate an important record of crustal shortening, flexure, and accumulation histories that are formed in isostatic response to the load created by FTB shortening (Angevine et al., 1990; Beaumont, 1981; Horton, 2018a; Jordan, 1981, 1995; Stockmal et al., 2007). The sedimentary history preserved in the Corque syncline provides a long-lived hinterland basin record of the duration of Andean mountain building, while the Chaco foreland basin contains only the youngest stage of Andean history (DeCelles and Horton, 2003; Horton, 2018a; McQuarrie et al., 2005). Incorporation of kinematic and flexural modelling allows us to investigate the structural controls on sedimentation and preservation. In our model, ramps through basement rocks double a crustal section of ~12–15 km, producing a much larger uplift signal (and thus topographic load) than shortening in the Paleozoic section, which typically repeats a ~3–5 km stratigraphic section. The basins produced due to basement loading (e.g. ~375–575 km, Fig. 5b) are broader and deeper than those produced by shortening in the Paleozoic section (e.g. ~50–225 km, Fig. 5b) because of the contrast in load imparted by larger ramps. Thus, the location and magnitude of crustal deflection (and thus accommodation space) is a function of the loads imparted by basement thrusts. These flexurally subsiding regions are filled with sediments shed from the FTB and elevated topography to the west and can form on both hinterland and foreland sides of the load.

Our model tracks the accumulation of sediments through time and is able to reproduce the thicknesses of synorogenic sedimentation found in Cenozoic basins throughout the region (Fig. 1c, Fig. 11). Sedimentation in the AP initiates as a flexurally-induced backbulge through foredeep environment prior to model initiation due to deformation in the proto-WC FTB (Fig. 2). This initial sedimentation, of only ~1.5 km, is a small portion of the overall preserved AP sedimentation in the Corque syncline (~15 km). Depending on the age of deformation in the EC this sedimentation predates 50–40 Ma and thus precedes or coincides with the deposition of the ~40 Ma Potoco Formation. As the FTB propagates eastward and shortening in the modern FTB initiates, the AP forms a flexurally induced hinterland basin that fills with Cenozoic synorogenic strata ('C', Fig. 5) sourced primarily off of the uplifted flank of the deep basement thrust sheet in the west (~615 km, Fig. 5b), with additional sedimentation possible from the east either from basement thrust sheet 1 (in sequence basement deformation) or basement thrust sheet 2 (a potential OOS basement thrust order) (Supplementary Fig. 4). In sequence basement thrust sheets would argue that the lower 4 km of Potoco Formation preserved in the eastern limb of the Corque syncline potentially were derived from the east. However, the predicted topography over the uplifted basement thrust 1 shows a steep westward facing topographic slope with limited drainage area defined by the uplifted topography. A steep western slope and a broad gentle eastern slope may limit sediment contribution from the east to within ~5–10 km of the uplift (Leeder, 1995) that is then eroded as the Corque syncline deforms. Alternatively, initial motion on basement thrust 2 limits the contribution to the Corque syncline from eastern sources by moving the potential source area farther to the east (Supplementary Fig. 4), promoting western-derived sediments in the lower 4 km of the Potoco Formation (Horton et al., 2001). The thickness and age range of the Potoco Fm is reproduced by our flexural model and matches the measured rate of sedimentation, within error, when we use our best fit velocities (Table 4, Fig. 11a), and the sediment sources predicted by our models do not conflict with the predominant eastward paleoflow measured in the lower 4 km of the Potoco Formation (Horton et al., 2001). The measured rate of sedimentation and sedimentary ages requires rapid subsidence and argues for more than just a foreland basin sedimentation history (Horton, 2018a) preserved in the AP. We argue that this rapid sedimentation rate and the Eocene to modern thickness of sedimentation in the AP is generated as a function of a double load imparted by two basement ramps. A double load, and thus rapid subsidence, is perhaps a unique feature of hinterland basins (Horton, 2012, 2018a).

Along the AP/EC border, thrust-induced exhumation associated with motion over the footwall of basement ramp 2 removes the Cretaceous through Silurian strata. Loading of the FTB due to continued uplift over a WC basement ramp (Fig. 5c) and eastward emplacement of basement thrust sheets in the EC and SA, as well as AP shortening, drives subsidence of the AP/EC between 25 Ma and present ('LP', Fig. 5e–h). Thus, our model reproduces the erosional and sedimentary history found in Lago Poopo (McQuarrie and DeCelles, 2001).

In the EC, the pre-Andean FTB in our model drove backbulge through forebulge sedimentation at the location of Morochata (Fig. 2). As deformation propagates eastward into the modern FTB, Morochata lies between the locus of deformation on the western edge due to basement thrust sheet emplacement, and the thin-skinned shortening in the Paleozoic cover to the east. Isostatic loading and erosion from this proximal thin-skinned thrusting initiated sedimentation in the Morochata basin east ('M', Fig. 5b). Initial loading from basement sheet 2 dominated the isostatic load, and the resulting sedimentation in the basin kept Morochata in a foredeep/wedgetop position. This sedimentation history of Morochata broadly matches the measured thicknesses, ages, and sedimentary environments of sediments preserved in measured sections along strike but farther to the south in the Camargo Syncline (Fig. 11c) (DeCelles and Horton, 2003).

On the far eastern edge of the EC, our model preserves basin sedimentation not found in the section at 18°S. These sedimentary strata formed initially in a backbulge location with restricted sedimentation, but as the FTB migrated eastward and increased subsidence in the region between Oligocene and early Miocene, the bulk of the sedimentation occurred in proximal foredeep environments similar and adjacent to Morochata ('I', Fig. 5b–d). Though this basin is not preserved at 18°S, similar captured Cretaceous through Miocene sedimentary basins (Incapampa (Fig. 1c) and Tarabuco) are found along strike south of this section (DeCelles and Horton, 2003; Horton, 2005). These basins are preserved in front of the hangingwall of the easternmost EC basement thrust sheet. These are separate from the Camargo, Torotoro, and Morochata basins, by a structural high of predominantly Ordovician age rocks (Horton, 2005) that place the Camargo, Torotoro, and Morochata basins behind (west) of the basement thrust sheet hangingwall cutoff (Eichelberger et al., 2013; McQuarrie, 2002). In geology of the region and in the kinematics of the original cross-section, the modelled basin remnant at the far eastern edge of the EC would have been erosionally removed though the uplift associated with fault-bend-fold hanging wall steepening (Suppe, 1983) of basement thrust 3, a deformation process *Move* is not able to model without perfectly flat décollements. The inability to reproduce this deformation, forces the basin to remain caught between the eastern basement thrust hanging wall and the SA basement thrust, a position that has preserved these basins in the fold-thrust belt farther to the south. The preservation of this basin argues for the basement ramp associated with basement thrust sheet 3 to be located further east. This would force the toe of the hangingwall of thrust sheet 3 farther under the EC/IAZ boundary, providing structural elevation allowing for erosional removal of the basin.

For the majority of the model time, our modelled modern FB (i.e. the SA) receives little to no subsidence due to its location far from the locus of shortening ('F', Fig. 5a-e). However, as SA shortening initiates in the Miocene, the bulk of the ~4.5 km of FB sediments form in response to a flexurally-driven foredeep driven by the SA basement thrust (Fig. 5f-h) predicting basal foreland basin sediments that are ~10 Ma. This lack of Paleocene and Eocene strata, as well as the thickness of produced Miocene synorogenic sedimentation, match the measured FB strata (Fig. 11) (Marshall et al., 1993; Marshall and Sempere, 1991; Uba et al., 2005, 2009).

The primary driver of loading and thus accommodation space throughout our model is the location and emplacement of basement thrusts. These exert a first-order control on accommodation space and the partitioning of basins.

5.3. Lateral variability in structure, kinematics and velocity

5.3.1. Structural and stratigraphic variability

Across the Bolivian Andes, many authors have noted lateral variability in age and location of strata exposed at the surface; as a result, they have interpreted subsurface structural changes in the geometry of the FTB to be the cause of these surface variations (Fig. 12) (e.g. Baby et al., 1995; Kley, 1999). The first order geometry of a FTB is set by preexisting structures, crustal weaknesses, and the sedimentary material available to deform (Boyer, 1995; McQuarrie and Ehlers, 2017; Mitra, 1997). In the Bolivian Andes, there are several pre-existing structural weaknesses that may have been reactivated or have driven significant variations is sedimentation imparting a control on FTB deformation and resulting in laterally varying map patterns: Late Permian-Jurassic rift structures (Sempere et al., 2002), Early Cretaceous rifting (Sempere et al., 1997), basement highs (Baby et al., 1994, 1995; Williams, 1995). These, in combination with changing tectonic, climatic, and transport conditions influenced the shape and contributed to the variability of the Paleozoic sedimentary basins (Baby et al., 1995; Sempere et al., 1997, 2002). Lateral variability in the sedimentary strata and basement geometry can alter what horizons act as ramps and flats.

The IAZ is broadly defined as the portion of the FTB whose rocks at the surface (primarily Devonian) require a marked change in structural elevation from the SA. This structural elevation is imparted by the easternmost, and thus most recent, basement thrust sheet (Kley, 1996, 1999; McQuarrie, 2002). As the FTB continues to deform and thrusts propagate outward to the SAZ, the rocks of the IAZ are uplifted and passively transported on this basement thrust sheet. Via a balanced cross-section, basement thrust sheets are restored to determine their ramp locations. These basement structures, both thrust sheets and ramps, exert a first order control on the location and expression of the IAZ.

At 18°S (Fig. 12,ii), Ordovician and Cambrian strata are at the surface in the IAZ (Fig. 12a). Topographically, the elevations along strike are relatively consistent and cannot explain the presence of deeper stratigraphy present at the surface. To the northwest of our study area, there is a southwest-northeast trending contact, perpendicular to fault orientation, between the Ordovician-Silurian and Devonian strata (Fig. 12,ii). This transition from Cambrian strata at the surface to Carboniferous and Permian strata at the surface ~75 km northwest illustrates a rapid decrease in structural elevation (Fig. 12a) [and erosion level (Fig. 13c)]. There is a similar decrease in structural elevation along strike to the southeast, where Carboniferous rocks are present again ~150 km southeast (Fig. 13c).

As a result of a series of coarsening upward sedimentary sequences (Baby et al., 1995; Sempere, 1995), there are multiple décollement levels which transfer slip and accommodate shortening at various stratigraphic levels in the Bolivian Andes. Between 15 and 17°S (Fig. 13b), the base of the Ordovician section acts as the décollement in both the SA and IAZ, with a secondary décollement at the bottom of the Devonian strata (McQuarrie et al., 2008a). At 18°S, the bottom of the Ordovician and Devonian sections are still décollements in the SA, however, the bottom of the Cambrian section is also a décollement (McQuarrie, 2002). At 19°S, the primary décollement has moved to the top of the Ordovician section in the SA, as the shallow dip and FB thickness does not permit carrying the additional stratigraphy (Eichelberger et al., 2013). The SA at 18°S are narrow, likely due to the edge of the Paleozoic basin and/or the Chapare basement high (Baby et al., 1994, 1995), which limited and promoted the propagation of the FTB into the foreland (i.e. a forward lateral boundary) and likely promoted the presence of exposed Cambrian rocks at the surface. This unique presence of Cambrian rocks in the map pattern requires a change in geometry to facilitate the increase in structural elevation required by these older, deeper rocks at the surface (Fig. 12d). The adjacent cross-sections show the basement thrust at the lowest décollement level either above or below the Ordovician (Eichelberger et al., 2013; McQuarrie et al., 2008a; Rak et al., 2017). These constraints require lateral structures, either in the hangingwall, footwall or both, between this study and the adjacent cross-sections in order to permit the variation in map pattern and cross-section geometry.

Fig. 13 highlights the location of the décollement and stratigraphy that is immediately above and below it along the border of the IAZ and SA (orange dashed line, Fig. 12a,b). The figure shows variations in stratigraphic thickness as well as marked changes in the hangingwall and footwall stratigraphy (Fig. 13a). From south to north, the décollement, between 19 and 18°S, changes from the top of a potentially thinner Ordovician section at 19°S to the top of the Silurian at 18°S A lateral footwall ramp separating these two sections can be ~1 km to ~3 km depending on if the thickness of the Ordovician changes gradually or abruptly (solid and dashed line between 19°S and 18°S, Fig. 13b). Between 18 and 15–17°S the décollement steps down (~1 km) to the top of the Ordovician. While variations in hangingwall stratigraphy from 19 and 18°S are minimal with both sections showing the basement cut off immediately above the décollement, hanging wall stratigraphy between 18 and 15–17°S shows a much more dramatic change from basement at 18°S to the Devonian section 15–17°S. This marked change in stratigraphy argues for a ~5 km hangingwall lateral ramp. The lateral ramp is highlighted in the map pattern at 17°S. In this location, the trend of fold and faults are northwest, perpendicular to the shortening direction, while the stratigraphy at the surface changes from Cambrian to Carboniferous strata over a 10–20 km distance perpendicular (i.e. with contacts parallel) to the shortening direction, and 90° to expected (and ubiquitous) stratigraphic changes which are generally parallel to the transport direction. Thus, the more deeply exposed stratigraphy at 17–18°S is a function of both a hanging wall geometry carrying basement rocks farther east than sections to the north as well as a change in the footwall geometry where the décollement above thinner Ordovician strata allows for less structural uplift and less exhumation to the south.

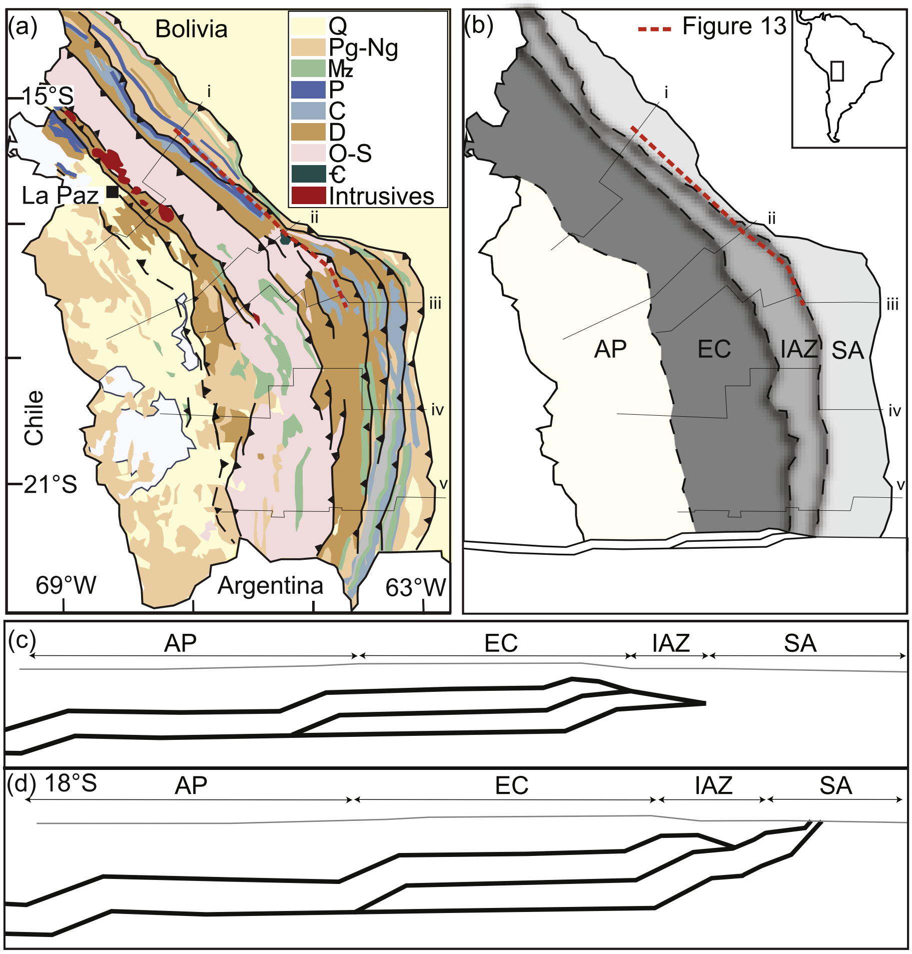

Fig. 12. (a) Simplified geologic map of Bolivia (modified from (Eichelberger et al., 2013; McQuarrie, 2002)); (b) Structural elevations due to basement thrusts and tectonogeomorphic zones (Paleozoic cover not shown; modified from (Kley, 1999; McQuarrie and DeCelles, 2001)); thin lines are locations of studies referenced herein (from N-S: (i) Rak et al., 2017 and McQuarrie et al., 2008a; (ii) McQuarrie, 2002, this study; (iii) Eichelberger et al., 2013; (iv) McQuarrie, 2002; (v) Anderson et al., 2017, 2018); simplified cross-sections highlighting basement (thick lines) and SA (thin lines) geometry: (c) representative of the majority of Bolivia; (d) representative of 18°S. Dashed line indicates approximate location of Fig. 13.

5.3.2. Kinematic variability

OOS faulting in this region of Bolivia was first proposed by Whipple and Gasparini (2014) based on the location and pattern of steep river channels (Ksn, a measure of channel slope normalized to drainage area). High Ksn values associated with active uplift and can be related to surface breaking thrust faults or uplift over subsurface ramps (Gasparini and Whipple, 2014; Kirby and Whipple, 2012; Wobus et al., 2006). Thus, high Ksn would be expected over the active basement ramp and at the deformation front in our model (if deformation was occurring in-sequence). However, the highest Ksn values located west of the deformation front are not collocated with our basement ramp. Instead, these high Ksn values are immediately west-southwest of the thrust that breaks the surfaces at ~20 km in our model (Fig. 10), providing support for an out-of-sequence thrust in this location. Our modelling results show that in-sequence deformation does not produce the best fit to measured data, and instead highlights the efficacy of an OOS model at reproducing the measured thermochronology (Fig. 6, Table 4). Our modelled OOS thrust is permitted by the map pattern and there are several mechanistic arguments in support of OOS thrusting in this portion of the Bolivian Andes, including focused erosion, either due to increased climatic effects or tectonically-controlled topographic driving orographic rainfall (Dahlen, 1990), and pre-existing structural controls limiting forward propagation of the FTB. Propagation of the thrust front is limited when more work is required to slip along the basal décollement than to ramp upsection (Boyer, 1995; Dahlen, 1990; Mitra, 1997). While it is possible that the high precipitation gradient in the region has focused erosional removal of material and promoted a hinterland increase in topography prior to further propagation, the modern-day high precipitation gradient could be an orographic response to OOS thrusting.

5.3.3. Variability of velocity along and across section

Many previous authors have proposed variable shortening rates in the central Andes (Anderson et al., 2018; Eichelberger et al., 2013; Elger et al., 2005; Hindle et al., 2005; Hindle and Burkhard, 1999; McQuarrie et al., 2005; Oncken et al., 2006; Rak et al., 2017). Spatial and temporal variation in shortening rate can be affected by convergence rate and coupling between the subducting and overriding plate (Babeyko and Sobolev, 2005; Horton, 2018a, 2018b), the angle and rate of slab subduction, possibly related to full or partial mantle convection (Faccenna et al., 2013; Royden, 1993; Schellart, 2017), an upper plate response to accumulation and loss of mantle lithosphere (DeCelles et al., 2009), and the lithologic and stratigraphic variability altering the work required to deform (Mitra, 1997). Rates of deformation have been determined from a variety of data sources, and initial velocity estimates in the Central Andes frequently relied on the San Juan del Oro surface (~10 Ma) to constrain the end of EC deformation, and the initiation of SA deformation (e.g. Gubbels et al., 1993). Sedimentation ages and rates are frequently used to constrain the timing of shortening (Echavarria et al., 2003; Espurt et al., 2008; Uba et al., 2009); however, poor age control (DeCelles and Horton, 2003) and the disconnect between age of sedimentation and age of deformation (Rak et al., 2017) can affect the reliability of these shortening rates. Newer methods of determining rates of deformation incorporate exhumation ages determined by low-temperature thermochronology (Anderson et al., 2018; Barnes et al., 2006, 2012; Lease et al., 2016; McQuarrie et al., 2008a), but require a cautious approach because the age of exhumation recorded by a given chronometer system may not be the age

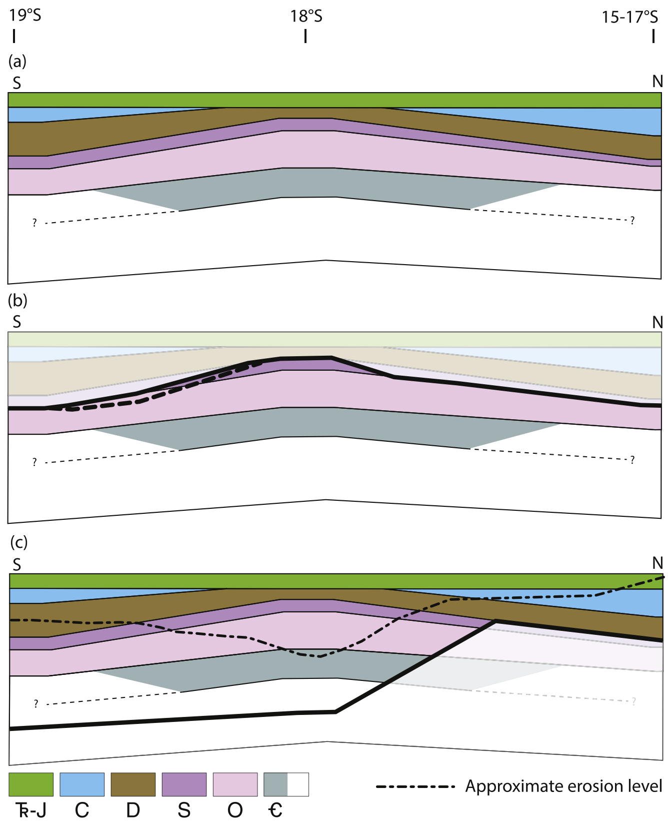

Fig. 13. Structural and Stratigraphic variation along the IAZ/SA boundary. Line of section along IAZ/SA border (Fig. 12). (a) initial stratigraphic variation in thickness between 15 and 17°S and 19°S (thicknesses measured from McQuarrie, 2002; McQuarrie et al., 2008a and Eichelberger et al., 2013. (b) depiction of footwall structure with alternate (dashed) geometry; (c) depiction of hangingwall structure and erosion level.

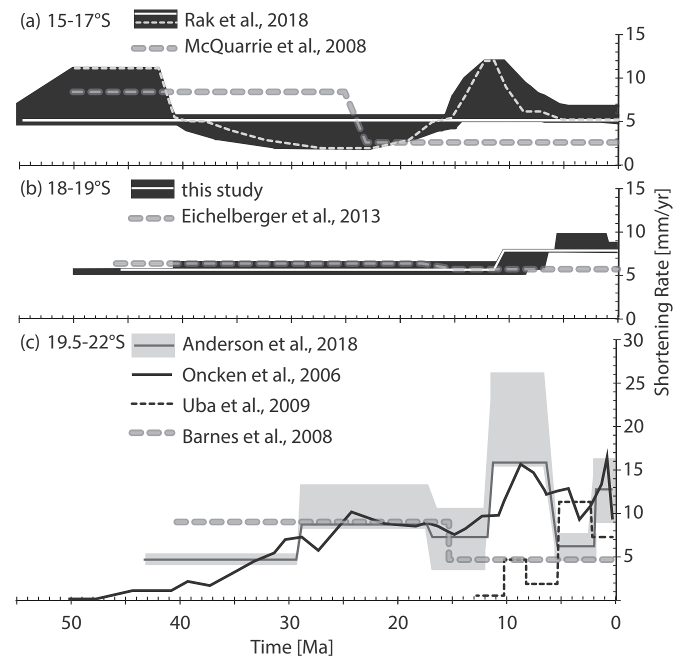

Fig. 14. Proposed shortening rates across Bolivia. (a,b,c) thick gray dashed line: bulk thermochronology data with AP, EC, and IAZ averaged shortening rate separate from SA shortening rate; (a,b) Black area acceptable velocity envelopes, white line selected velocity models from coupled thermokinematic modelling; (c) gray line estimated shortening rate with light gray area error estimate on shortening rate(Anderson et al., 2018); black line (Oncken et al., 2006), from thermochronology, sedimentology, and kinematic restoration. Black dashed line SA shortening rate (Uba et al., 2009) from sedimentology. Note different vertical axis limits on (c).

of deformation. This is particularly important in the central Andean FTB as exhumation over basement ramps provides a first-order control on exhumation and thus can overwrite an initial deformation history (Rak et al., 2017; this study). Young AFT samples from the IAZ and AFT (at 18°S) that record rapid exhumation at 6 ± 2 Ma have been used to argue for an initiation of SA deformation at this time (Lease et al., 2016); however, as shown in Fig. 5f-g, exhumation in the IAZ occurs again at ~10 Ma due to uplift over basement structures, and the resulting IAZ and SA modelled ages fall within the published AFT thermochronology range of 2–9 Ma (Fig. 10f). The period of rapid exhumation is not directly equivalent to the start of IAZ or SA deformation, as exhumation induced by the emplacement over the active basement ramp associated with SA shortening overwrites the initial IAZ ages such that the measured thermochronology ages only record the last stage of shortening.

Our model results for 18°S suggests that the shortening rate associated with initial Andean deformation was relatively stable at ~5.2–6.8 mm/yr during EC, IAZ, and the majority of AP emplacement (~50 to ~12–9 Ma), and that shortening rate increased to 8–10 mm/yr between 12 and 9 Ma (black, Fig. 14b). The shortening rate during initial Andean deformation is roughly in agreement with the ~7 mm/yr approximate shortening rate predicted from balanced cross-section and low-temperature thermochronology just to the south (19°S, Eichelberger et al., 2013, Fig. 14b). In northern Bolivia (15–17°S), the acceptable velocity envelope identified in previous studies incorporating thermokinematic modelling permits a constant 5–7 mm/yr velocity over the entire 50–55 Ma shortening history, with possible windows of increased shortening rates between 50 and 42 Ma (up to 11 mm/yr) and between 15 and 5 Ma (up to 12 mm/yr) (Fig. 14a) (Rak et al., 2017). This pulse of rapid SA deformation starts earlier than our preferred shortening rate (white line, Fig. 14b). To match measured cooling ages and basin data, SA shortening in northern Bolivia has to decrease to 7 mm/yr from ~5 Ma to present. In contrast, shortening rates remain at 8–10 mm/yr to the present in our study region suggesting lateral variability in shortening rates in the SA.

Authors incorporating balanced cross-section and low-temperature thermochronology, approximate the shortening rate at 19.5°S to be 9 mm/yr from ~40–15 Ma during EC, AP, and IAZ shortening (Fig. 14c, Barnes et al., 2008) with rates decreases to ~5 mm/yr from 15 Ma to present during SA shortening (Barnes et al., 2008). However, a detailed study incorporating U-Pb dating and sedimentology in the SA between 19.5 and 21.5°S found that SA shortening may have initiated closer to ~13–10 Ma at rates increasing up to ~11 mm/yr between 5 and 3 Ma (Uba et al., 2009). In far south Bolivia (20.5–22°S), authors proposed a FTB shortening rate incorporating low-temperature thermochronology exhumation ages, sedimentation, and balanced cross-section deformation estimates (Anderson et al., 2018; Oncken et al., 2006). The proposed rate by Oncken et al. (2006) increases from ~0 mm/yr at 50 Ma, to ~7 ± 2 mm/yr from 33 to 10 Ma, and finally to 13 ± 4 mm/yr between 10 Ma and present (Fig. 14c). Anderson et al. (2018) proposed that deformation occurred in a series of pulses, with a background shortening rate of ~3–5 mm/yr, and pulses of 9–13 mm/yr, 15–27 mm/yr and 9–16 mm/yr during 28–18 Ma, 11–7 Ma, and 2–0 Ma, respectively (Fig. 14c). The proposed shortening rates are strongly influenced by the San Juan del Oro paleosurface and synchronous IAZ populations of AFT and AHe ages (10–20 Ma, Anderson et al., 2018). Due to these factors, the proposed timing pulses may overpredict shortening rate for ~10 Ma to present compared to 15–17°S and 18°S. Synchronous populations of thermochronometers from multiple thermochronometer systems in the IAZ at 21–22°S require that a large exhumation event occurred (McQuarrie and Ehlers, 2015, 2017) at ~10 Ma and potentially as early as 20 Ma, likely due to the initiation of motion on the most recent basement ramp with associated uplift and exhumation (Rak et al., 2017; this study). A 13–10 Ma initiation of SAZ deformation would produce 4–8 mm/yr rate of deformation, with possible faster rates from 2 Ma to present.

6. Conclusions

The research presented here highlights the importance of thermal, flexural, and kinematic modelling as additional constraints to test the validity of balanced cross-sections. While low exhumation amounts can present additional challenges, the methodology presented herein allows a mensurable link between balanced cross-sections, synorogenic sedimentation, and thermal histories. Derivation of particle paths from detailed flexural and kinematic models allow us to quantitatively link balanced cross-sections with modelled thermal ages and the formation of sedimentary basins through time which they produce. The location of a basement thrust ramp proposed by McQuarrie (2002) resulted in over-erosion of the sedimentary cover, while relocation of this ramp successfully replicated surface geology.

Significantly low AP elevations predicted by initial flexural modelling required the incorporation of a long-wavelength, imposed uplift to prevent excess subsidence and raise the AP to its modern elevations. Inadequately thick SA deposits additionally argue for imposed subsidence to increase the accommodation space available. The requirement for imposed subsidence in the foreland may suggest the impartation of a signal due to viscous coupling between the mantle wedge and subducting oceanic plate (DeCelles, 2012). The need for imposed uplift of the AP could be representative of mantle delamination (Garzione et al., 2006), Airy isostasy attainment (Beck et al., 1996), and/or lower crustal flow (Eichelberger et al., 2015; Isacks, 1988; Lamb, 2011), and is consistent with arguments to maintain elevation in the absence of deformation-induced uplift (Rak et al., 2017).

Mismatch between modelled and published ages informs us as to how cross-section kinematics and deformation rates can be revised to create a more accurate solution to known constraints. In-sequence kinematics and constant (~5.8 mm/yr) deformation rates resulted in a mismatch between published and modelled ZHe data, while increasing SA deformation rates and revising the SA kinematic order to incorporate OOS thrusting provides a necessary pause in uplift and exhumation over doubled SA ramps in order to match published ZHe data. While the geometry and kinematics set the pattern of permissible cooling ages, changes in velocity controls the absolute ages recorded and changes to radiogenic heat production alter which patterns of cooling are recorded in which thermochronometer. Our model is insensitive to model start times tested (50, 45, 40 Ma), and requires at least 5.2 mm/yr shortening rate during EC emplacement. While a peak velocity of up to 12 mm/yr during initial SA emplacement, slowing to ~6 mm/yr at present, provides an acceptable fit (> 55% fit), the best fit (> 65% fit) has deformation rates of 8–10 mm/yr during the entire SA emplacement.

Acknowledgments

The authors would like to thank Guest Editor Christoph Von Hagke and reviewers Joel Saylor and Ryan Anderson for their comments and suggestions that have greatly improved this manuscript. Supporting data are included in the supporting information file; any additional data or information are available through contacting VMB Parks (email: vmbparks@gmail.com). This work was supported by NASA headquarters under the NASA Earth and Space Science Fellowship program - Grant 80NSSC17K0388. We acknowledge and thank Midland Valley and Petex for support and use of the program *Move.* This manuscript benefitted from thoughtful discussions over the years with Paul Eizenhöfer, Mary Braza, Chloë Glover, and Brad Parks. T.A. Ehlers and Willi Kappler (University of Tübingen) are thanked for support with conducting modelling simulations and providing the modified version of *Pecube* that can be coupled to *2D Move* restoration files.

Appendix A. Supplementary data

Supplementary data to this article can be found online at https://doi.org/10.1016/j.tecto.2019.06.008.

References

Almendral, A., Robles, W., Parra, M., Mora, A., Ketcham, R.A., Raghib, M., 2015. FetKin: Coupling kinematic restorations and temperature to predict thrusting, exhumation histories, and thermochronometric ages. Am. Assoc. Pet. Geol. Bull. 99, 1557–1573. https://doi.org/10.1306/07071411112.

Anderson, R.B., Long, S.P., Horton, B.K., Calle, A.Z., Ramirez, V., 2017. Shortening and structural architecture of the Andean foldthrust belt of southern Bolivia (21°S): Implications for kinematic development and crustal thickening of the central Andes. Geosphere 13, 538–558. https://doi.org/10.1130/GES01433.1.

Anderson, R.B., Long, S.P., Horton, B.K., Thomson, S.N., Calle, A.Z., Stockli, D.F., 2018. Orogenic wedge evolution of the central Andes, Bolivia (21°S): Implications for Cordilleran cyclicity. Tectonics 37, 3577–3609. https://doi.org/10.1029/2018TC005132.

Angevine, C.L., Heller, P.L., Paola, C., 1990. Quantitative Sedimentary Basin Modelling, Continuing Education, Course Note Series #32. AAPG. ISBN13: 9780891811800.

Armijo, R., Lacassin, R., Coudurier-Curveur, A., Carrizo, D., 2015. Coupled tectonic evolution of Andean orogeny and global climate. Earth-Science Rev. 143, 1–35. https://doi.org/10.1016/j.earscirev.2015.01.005.

Ashwal, L.D., Morgan, P., Kelley, S.A., Percival, J.A., 1987. Heat production in an Archean crustal profile and implications for heat flow and mobilization of heat-producing elements. Earth Planet. Sci. Lett. 85, 439–450. https://doi.org/10.1016/0012-821X(87)90139-7.

Babeyko, A.Y., Sobolev, S. V., 2005. Quantifying different modes of the late Cenozoic shortening in the central Andes. Geology 33, 621–624. doi:1130/G21126.1.

Baby, P., Specht, M., Oller, J., Montemurro, G., Colletta, B., Letouzey, J., 1994. The Boomerang-Chapare transfer zone (recent oil discovery trend in Bolivia): structural interpretation and experimental approach. In: Roure, F., Ellouz, N., Shein, V.S., Skvortsov, I. (Eds.), Geodynamic Evolution of Sedimentary Basins, International Symposium, Moscow. Paris, pp. 203–218.

Baby, P., Moretti, I., Guillier, B., Limachi, R., Mendez, E., Oller, J., Specht, M., 1995. Petroleum system of the Northern and Central Bolivian sub-Andean Zone. In: Tankard, A.J., Suarez S., R., H.J., Welsink (Eds.), Petroleum Basins of South America: AAPG Memoir 62, pp. 445–458 (ISBN: 0891813411).

Baby, P., Rochat, P., Mascle, G., Herail, G., 1997. Neogene shortening contribution to crustal thickening in the back arc of the Central Andes. Geology 25, 883–886. https://doi.org/10.1130/0091-7613(1997)025 < 0883:NSCTCT > 2.3.CO;2.

Barnes, J.B., Ehlers, T.A., 2009. End member models for Andean Plateau uplift. Earth-Science Rev 97, 105–132. https://doi.org/10.1016/j.earscirev.2009.08.003.

Barnes, J.B., Ehlers, T.A., McQuarrie, N., O'Sullivan, P.B., Pelletier, J.D., 2006. Eocene to recent variations in erosion across the central Andean fold-thrust belt, northern Bolivia: implications for plateau evolution. Earth Planet. Sci. Lett. 248, 103–118. https://doi.org/10.1016/j.epsl.2006.05.018.

Barnes, J.B., Ehlers, T.A., McQuarrie, N., O'Sullivan, P.B., Tawackoli, S., 2008. Thermochronometer record of central Andean Plateau growth, Bolivia (19.5°S). Tectonics 27. https://doi.org/10.1029/2007TC002174.

Barnes, J.B., Ehlers, T.A., Insel, N., McQuarrie, N., Poulsen, C.J., 2012. Linking orography, climate, and exhumation across the central Andes. Geology 40, 1135–1138. https://doi.org/10.1130/G33229.1.

Beaumont, C., 1981. Foreland Basins. R. Astron. Soc. Geophys. J. 65, 291–329. https://doi.org/10.1111/j.1365-246X.1981.tb02715.x.

Beck, S.L., Zandt, G., Myers, S.C., Wallace, T.C., Silver, P.G., Drake, L., 1996. Crustal thickness variations in the central Andes. Geology 24, 407–410. https://doi.org/10.1130/0091-7613(1996)024%3C0407:CTVITC%3E2.3.CO;2.

Boyer, S.E., 1995. Sedimentary basin taper as a factor controlling the geometry and advance of thrust belts. Am. J. Sci. https://doi.org/10.2475/ajs.295.10.1220.

Boyer, S.E., Elliot, D., 1982. Thrust Systems. Am. Asoc. Petrol. Geol. Bull. 66, 1196–1230.

Braun, J., 2002. Quantifying the effect of recent relief changes on age-elevation relationships. Earth Planet. Sci. Lett. 200, 331–343. https://doi.org/10.1016/S0012-821X(02)00638-6.

Braun, J., 2003. Pecube: a new finite-element code to solve the 3D heat transport equation including the effects of a time-varying, finite amplitude surface topography. Comput. Geosci. 29, 787–794. https://doi.org/10.1016/S0098-3004(03)00052-9.

Brooks, B.A., Bevis, M., Whipple, K.X., Ramon Arrowsmith, J., Foster, J., Zapata, T., Kendrick, E., Minaya, E., Echalar, A., Blanco, M., Euillades, P., Sandoval, M., Smalley, R.J., 2011. Orogenic-wedge deformation and potential for great earthquakes in the central Andean backarc. Nat. Geosci. 4, 380–383. https://doi.org/10.1038/ngeo1143.

Calle, A.Z., Horton, B.K., Limachi, R., Stockli, D.F., Uzeda-Orellana, G.V., Anderson, R.B., Long, S.P, 2018. Cenozoic provenance and depositional record of the Subandean foreland basin during growth and advance of the central Andean fold-thrust belt, southern Bolivia. In: Zamora, G., McClay, K., V.R. (Eds.), Petroleum Basins and Hydrocarbon Potential of the Andes of Peru and Bolivia. American Association of Petroleum Geologists Memoir 117, pp. 459–506. https://doi.org/10.1306/13622132M1173777.

Castelluccio, A., Andreucci, B., Zattin, M., Ketcham, R.A., Jankowski, L., Mazzoli, S., Szaniawski, R., 2015. Coupling sequential restoration of balanced cross-sections and low-temperature thermochronometry: the case study of the Western Carpathians. Lithosphere 7, 367–378. https://doi.org/10.1130/L436.1.
Catuneanu, O., 2004. Retroarc foreland systems—Evolution through time. J. African Earth Sci. 38, 225–242. https://doi.org/10.1016/j.jafrearsci.2004.01.004.
Chapman, J.B., Carrapa, B., Ballato, P., DeCelles, P.G., Worthington, J., Oimahmadov, I., Gadoev, M., Ketcham, R.A., 2017. Thermokinematic Modelling of Shortening in the Tajik Fold and Thrust Belt: Implications for Intracontinental Subduction beneath the Pamir Mountains. pp. 1450–1471. https://doi.org/10.1130/B31730.1.
Dahlen, F.A., 1990. Critical Taper Model of Fold-And-Thrust Belts and Accretionary Wedges. Annu. Rev. Earth Planet. Sci. 18, 55–99. https://doi.org/10.1146/annurev.ea.18.050190.000415.
DeCelles, P.G., 2012. Foreland basin systems revisited: Variations in response to tectonic setting. In: Busby, C., Azor, A. (Eds.), Tectonics of Sedimentary Basins: Recent Advances. Blackwell, Oxford, UK, pp. 405–426. https://doi.org/10.1002/9781444347166.ch20.
DeCelles, P.G., Horton, B.K., 2003. Early to middle Tertiary foreland basin development and the history of Andean Early to middle Tertiary foreland basin development and the history of Andean crustal shortening in Bolivia. Geol. Soc. Am. Bull. 58–77. https://doi.org/10.1130/0016-7606(2003)115.
DeCelles, P.G., Ducea, M.N., Kapp, P., Zandt, G., 2009. Cyclicity in Cordilleran orogenic systems. Nat. Geosci. 2, 251–257. https://doi.org/10.1038/ngeo469.
Donelick, R.A., O'Sullivan, P.B., Ketcham, R.A., 2005. Apatite fission-track analysis. Rev. Mineral. Geochemistry 58, 49–94. https://doi.org/10.2138/rmg.2005.58.3.
Echavarria, L., Hernandez, R., Allmendinger, R., Reynolds, J., 2003. Subandean thrust and fold belt of northwestern Argentina: geometry and timing of the Andean evolution. Am. Asoc. Petrol. Geol. Bull. 87, 965–985. https://doi.org/10.1306/01200300196.
Ege, H., 2004. Exhumations-und Hebungsgeschichte der zentralen Anden in Südbolivien durch Spaltspur-Thermochoronolgie an Apatit.
Ege, H., Sobel, E.R., Scheuber, E., Jacobshagen, V., 2007. Exhumation history of the southern Altiplano plateau (southern Bolivia) constrained by apatite fission track thermochronology. Tectonics 26, 1–24. https://doi.org/10.1029/2005TC001869.
Ehlers, T.A., 2005. Crustal thermal processes and the interpretation of thermochronometer data. Rev. Mineral. Geochemistry 58, 315–350. https://doi.org/10.2138/rmg.2005.58.12.
Ehlers, T.A., Farley, K.A., 2003. Apatite (U-Th)/He thermochronometry: methods and applications to problems in tectonic and surface processes. Earth Planet. Sci. Lett. 206, 1–14. https://doi.org/10.1016/S0012-821X(02)01069-5.
Eichelberger, N., McQuarrie, N., Ehlers, T.A., Enkelmann, E., Barnes, J.B., Lease, R.O., 2013. New constraints on the chronology, magnitude, and distribution of deformation within the central Andean orocline. Tectonics 32, 1432–1453. https://doi.org/10.1002/tect.20073.
Eichelberger, N., McQuarrie, N., Ryan, J., Karimi, B., Beck, S.L., Zandt, G., 2015. Evolution of crustal thickening in the central Andes, Bolivia. Earth Planet. Sci. Lett. 426, 191–203. https://doi.org/10.1016/j.epsl.2015.06.035.
Elger, K., Oncken, O., Glodny, J., 2005. Plateau-style accumulation of deformation: Southern Altiplano. Tectonics 24, 1–19. https://doi.org/10.1029/2004TC001675.
Erdös, Z., Van Der Beek, P., Huismans, R.S., 2014. Evaluating balanced section restoration with thermochronology data: a case study from the Central Pyrenees. Tectonics 33, 617–634. https://doi.org/10.1002/2013TC003481.
Espurt, N., Brusset, S., Baby, P., Hermoza, W., Bolaños, R., Uyen, D., Déramond, J., 2008. Paleozoic structural controls on shortening transfer in the Subandean foreland thrust sytem, Ene and southern Ucayali basins, Peru. Tectonics 27, 1–21. https://doi.org/10.1029/2007TC002238.
Faccenna, C., Becker, T.W., Conrad, C.P., Husson, L., 2013. Mountain building and mantle dynamics. Tectonics 32, 80–93. https://doi.org/10.1029/2012TC003176.
Garzione, C.N., Molnar, P., Libarkin, J.C., MacFadden, B.J., 2006. Rapid late Miocene rise of the Bolivian Altiplano: evidence for removal of mantle lithosphere. Earth Planet. Sci. Lett. 241, 543–556. https://doi.org/10.1016/j.epsl.2005.11.026.
Garzione, C.N., Hoke, G.D., Libarkin, J.C., Withers, S., MacFadden, B., Eiler, J., Ghosh, P., Mulch, A., 2008. Rise of the Andes. Science 320, 1304–1307. https://doi.org/10.1126/science.1148615.
Garzione, C.N., Auerbach, D.J., Jin-Sook Smith, J., Rosario, J.J., Passey, B.H., Jordan, T.E., Eiler, J.M., 2014. Clumped isotope evidence for diachronous surface cooling of the Altiplano and pulsed surface uplift of the Central Andes. Earth Planet. Sci. Lett. 393, 173–181. https://doi.org/10.1016/j.epsl.2014.02.029.
Garzione, C.N., McQuarrie, N., Perez, N.D., Ehlers, T.A., Beck, S.L., Kar, N., Eichelberger, N., Chapman, A.D., Ward, K.M., Ducea, M.N., Lease, R.O., Poulsen, C.J., Wagner, L.S., Saylor, J.E., Zandt, G., Horton, B.K., 2017. Tectonic evolution of the Central Andean Plateau and implications for the growth of Plateaus. Annu. Rev. Earth Planet. Sci. 45, 529–559. https://doi.org/10.1146/annurev-earth-063016-020612.
Gasparini, N.M., Whipple, K.X., 2014. Diagnosing climatic and tectonic controls on topography: Eastern flank of the northern Bolivian Andes. Lithosphere 6, 230–250. https://doi.org/10.1130/L322.1.
Gillis, R.J., Horton, B.K., Grove, M., 2006. Thermochronology, geochronology, and upper crustal structure of the Cordillera Real: implications for Cenozoic exhumation of the central Andean plateau. Tectonics 25, 1–22. https://doi.org/10.1029/2005TC001887.
Gilmore, M.E., McQuarrie, N., Eizenhöfer, P., Ehlers, T.A., 2018. Testing the effects of topography, geometry and kinematics on modeled thermochronometer cooling ages in the eastern Bhutan Himalaya. Solid Earth 9, 599–627. https://doi.org/10.5194/se-9-599-2018.
Gonfiantini, R., Roche, M., Olivry, J., Fontes, J., Maria, G., 2001. The altitude effect on the isotopic composition of tropical rains. Chem. Geol. 181, 147–167. https://doi.org/10.1016/S0009-2541(01)00279-0.
Gotberg, N., McQuarrie, N., Caillaux, V.C., 2010. Comparison of crustal thickening budget and shortening estimates in southern Peru (12-14S): implications for mass balance and rotations in the “Bolivian orocline”. Bull. Geol. Soc. Am. 122, 727–742. https://doi.org/10.1130/B26477.1.
Gubbels, T.L., Isacks, B.L., Farrar, E., 1993. High-level surfaces, plateau uplift, and foreland development. Bolivian central Andes. Geology 21, 695–698. https://doi.org/10.1130/0091-7613(1993)021 < 0695:HLSPUA > 2.3.CO;2.
Guenthner, W.R., Reiners, P.W., Ketcham, R.A., Nasdala, L., Giester, G., 2013. Helium diffusion in natural zircon: radiation damage, anisotropy, and the interpretation of zircon (U-TH)/He thermochronology. Am. J. Sci. 313, 145–198. https://doi.org/10.2475/03.2013.01.
Gurnis, M., 1993. Depressed continental hypsometry behind oceanic trenches: a clue to subduction controls on sea-level change. Geology 21, 29–32. https://doi.org/10.1130/0091-7613(1993)021 < 0029:DCHBOT > 2.3.CO;2.
Hatcher, R.D.J., Hooper, R.J., 1992. Evolution of crystalline thrust sheets in the internal parts of mountain chains. In: Thrust Tectonics. Chapman & Hall, pp. 217–233. ISBN13: 9789401130660. https://doi.org/10.1007/978-94-011-3066-0.
Heier, K.S., Adams, J.A.S., 1965. Concentration of radioactive elements in deep crustal material. Geochim. Cosmochim. Acta 29, 53–61. https://doi.org/10.1016/0016-7037(65)90078-5.
Henry, S.G., Pollack, H.N., 1988. Terrestrial heat flow above the Andean Subduction Zone in Bolivia and Peru. J. Geophys. Res. Solid Earth 93, 15153–15162. https://doi.org/10.1029/jb093ib12p15153.
Hindle, D., Burkhard, M., 1999. Strain, displacement and rotation associated with the formation of curvature in fold belts; the example of the Jura arc. J. Struct. Geol. 21, 1089–1101. https://doi.org/10.1016/S0191-8141(99)00021-8.
Hindle, D., Kley, J., Oncken, O., Sobolev, S., 2005. Crustal balance and crustal flux from shortening estimates in the Central Andes. Earth Planet. Sci. Lett. 230, 113–124. https://doi.org/10.1016/j.epsl.2004.11.004.
Horton, B.K., 2005. Revised deformation history of the central Andes: inferences from Cenozoic foredeep and intermontane basins of the Eastern Cordillera, Bolivia. Tectonics 24https://doi.org/10.1029/2003TC001619. n/a-n/a.
Horton, B.K., 2012. Cenozoic evolution of Hinterland Basins in the Andes and Tibet. In: Busby, C., Azor, A. (Eds.), Tectonics of Sedimentary Basins: Recent Advances. Blackwell Publishing Ltd, pp. 427–444. https://doi.org/10.1002/9781444347166.ch21.
Horton, B.K., 2018a. Sedimentary record of Andean mountain building. Earth-Science Rev 178, 279–309. https://doi.org/10.1016/j.earscirev.2017.11.025.
Horton, B.K., 2018b. Tectonic Regimes of the Central and Southern Andes: responses to Variations in plate coupling during subduction. Tectonics 37, 402–429. https://doi.org/10.1002/2017TC004624.
Horton, B.K., Hampton, B.A., Waanders, G.L., 2001. Paleogene synorogenic sedimentation in the Altiplano plateau and implications for initial mountain building in the Central Andes. Bull. Geol. Soc. Am. 113, 1387–1400. https://doi.org/10.1130/0016-7606(2001)113 < 1387:PSSITA > 2.0.CO;2.
Horton, B.K., Hampton, B.A., Lareau, B.N., Baldellon, E., 2002. Tertiary provenance history of the northern and central Altiplano (Central Andes, Bolivia); a detrital record of plateau-margin tectonics. J. Sediment. Res. 72, 711–726. https://doi.org/10.1306/020702720711.
Isacks, B.L., 1988. Uplift of the Central Andean Plateau and bending of the Bolivian orocline. J. Geophys. Res. 93, 3211–3231. https://doi.org/10.1029/JB093iB04p03211.
Jaupart, C., Mareschal, J.C., 2011. Heat Generation and Transport in the Earth. Cambridge University Press, New York (ISBN13: 9780521894883).
Jaupart, C., Mareschal, J.C., Iarotsky, L., 2016. Radiogenic heat production in the continental crust. Lithos 262, 398–427. https://doi.org/10.1016/j.lithos.2016.07.017.
Jordan, T.E., 1981. Thrust loads and foreland basin evolution, Cretaceous, Western United States. Am. Asoc. Petrol. Geol. Bull. 65, 2506–2520. https://doi.org/10.1306/03B599F4-16D1-11D7-8645000102C1865D.
Jordan, T.E., 1995. Retroarc Foreland and Related Basins. In: Ingersoll, R.V., Busby, C.J. (Eds.), Tectonics of Sedimentary Basins. Blackwell Science, pp. 331–362 (ISBN: 0865422451).
Kennan, L., Lamb, S., Rundle, C., 1995. K-Ar dates from the Altiplano and Cordillera Oriental of Bolivia: implicaitons for Cenozoic stratigraphy and tectonics. J. S. Am. Earth Sci. 8, 163–186. https://doi.org/10.1016/0895-9811(95)00003-X.
Ketcham, R.A., 1996. Distribution of heat-producing elements in the upper and middle crust of southern and west central Arizona: evidence from the core complexes. J. Geophys. Res. Solid Earth 101, 13611–13632. https://doi.org/10.1029/96JB00664.
Kirby, E., Whipple, K.X., 2012. Expression of active tectonics in erosional landscapes. J. Struct. Geol. 44, 54–75. https://doi.org/10.1016/j.jsg.2012.07.009.
Kley, J., 1996. Transition from basement-involved to thin-skinned thrusting in the Cordillera Oriental of southern Bolivia. Tectonics 15, 763. https://doi.org/10.1029/95TC03868.
Kley, J., 1999. Geologic and geometric constraints on a kinematic model of the Bolivian orocline. J. S. Am. Earth Sci. 12, 221–235. https://doi.org/10.1016/S0895-9811(99)00015-2.
Kley, J., Monaldi, C.R., Salfity, J.A., 1999. Along-strike segmentation of the Andean foreland: causes and consequences. Tectonophysics 301, 75–94. https://doi.org/10.1016/S0040-1951(98)90223-2.
Lamb, S., 2011. Did shortening in thick crust cause rapid Late Cenozoic uplift in the northern Bolivian Andes? J. Geol. Soc. Lond. 168, 1079–1092. https://doi.org/10.1144/0016-76492011-008.
Lamb, S., Hoke, L., 1997. Origin of the high plateau in the Central Andes, Bolivia, South America. Tectonics 16, 623–649. https://doi.org/10.1029/97TC00495.
Lease, R.O., Ehlers, T.A., Enkelmann, E., 2016. Large along-strike variations in the onset

of Subandean exhumation: implications for Central Andean orogenic growth. Earth Planet. Sci. Lett. 451, 62–76. https://doi.org/10.1016/j.epsl.2016.07.004.
Leeder, M.R., 1995. Continental Rifts and Proto-Oceanic Rift Troughs. In: Ingersoll, R.V., Busby, C.J. (Eds.), Tectonics of Sedimentary Basins. Blackwell Science, pp. 119–148 (ISBN: 0865422451).
Leier, A.L., McQuarrie, N., Horton, B.K., Gehrels, G.E., 2010. Upper Oligocene Conglomerates of the Altiplano, Central Andes: the record of deposition and deformation along the margin of a Hinterland Basin. J. Sediment. Res. 80, 750–762. https://doi.org/10.2110/jsr.2010.064.
Leier, A., McQuarrie, N., Garzione, C.N., Eiler, J., 2013. Stable isotope evidence for multiple pulses of rapid surface uplift in the central Andes, Bolivia. Earth Planet. Sci. Lett. 371–372, 49–58. https://doi.org/10.1016/j.epsl.2013.04.025.
Mareschal, J.C., Jaupart, C., 2013. Radiogenic heat production, thermal regime and evolution of continental crust. Tectonophysics 609, 524–534. https://doi.org/10.1016/j.tecto.2012.12.001.
Marshall, L.G., Sempere, T., 1991. The Eocene to Pleistocene Vertebrates of Bolivia and their stratigraphic context: a review. In: Suarez-Suruco, R. (Ed.), Fosiles y Facies de Bolivia Vertebrados. Rev. Tec. Yac. Petrol. Fis. Bolivia, pp. 631–652.
Marshall, L.G., Sempere, T., Gayet, M., 1993. The Petaca (Late Oligocene–Middle Miocene) and Yecua (Late Miocene) formations of the Subandean Chaco basin, Bolivia and their tectonic significance. Doc. du Lab. Geol. Lyon 125, 291–301.
McQuarrie, N., 2002. The kinematic history of the central Andean fold-thrust belt, Bolivia: implications for building a high plateau. Bull. Geol. Soc. Am. 114, 950–963. https://doi.org/10.1130/0016-7606(2002)114<0950:TKHOTC>2.0.CO;2.
McQuarrie, N., Davis, G.H., 2002. Crossing the several scales of strain-accomplishing mechanisms in the hinterland of the central Andean fold-thrust belt, Bolivia. J. Struct. Geol. 24, 1587–1602. https://doi.org/10.1016/S0191-8141(01)00158-4.
McQuarrie, N., DeCelles, P.G., 2001. Geometry and structural evolution of the central Andean. Tectonics 20, 669–692. https://doi.org/10.1029/2000TC001232.
McQuarrie, N., Ehlers, T.A., 2015. Influence of thrust belt geometry and shortening rate on thermochronometer cooling ages: Insights from thermokinematic and erosion modelling of the Bhutan Himalaya. Tectonics 34, 1–25. https://doi.org/10.1002/2014TC003783.
McQuarrie, N., Ehlers, T.A., 2017. Techniques for understanding fold-thrust belt kinematics, and thermal evolution. In: Law, R.D., Thigpen, J.R., Merschat, A.J., Stowell, H.H. (Eds.), Linkages and Feedbacks in Orogenic Systems: Geological Society of America Memoir. 213. pp. 1–30. https://doi.org/10.1130/2017.1213(02).
McQuarrie, N., Horton, B.K., Zandt, G., Beck, S.L., DeCelles, P.G., 2005. Lithospheric evolution of the Andean fold–thrust belt, Bolivia, and the origin of the central Andean plateau. Tectonophysics 399, 15–37. https://doi.org/10.1016/j.tecto.2004.12.013.
McQuarrie, N., Barnes, J.B., Ehlers, T.A., 2008a. Geometric, kinematic, and erosional history of the central Andean Plateau, Bolivia (15–17°S). Tectonics 27. https://doi.org/10.1029/2006TC002054.
McQuarrie, N., Ehlers, T.A., Barnes, J.B., Meade, B., 2008b. Temporal variation in climate and tectonic coupling in the central Andes. Geology 36, 999–1002. https://doi.org/10.1130/G25124A.1.
Mitra, G., 1997. Evolution of salients in a fold- and-thrust belt: the effects of sedimentary basin geometry, strain distribution and critical taper. In: Sengupta, S. (Ed.), Evolution of Geological Structures in Micro- to Macro-Scales. Springer Netherlands, Dordrecht, pp. 59–90. https://doi.org/10.1007/978-94-011-5870-1_5.
Mitra, G., Boyer, S.E., 1986. Energy balance and deformation mechanisms of duplexes. J. Struct. Geol. 8, 291–304. https://doi.org/10.1016/0191-8141(86)90050-7.
Mitrovica, J.X., Beaumont, C., Jarvis, G.T., 1989. Tilting of continental interiors by the dynamical effects of subduction. Tectonics 8, 1079–1094. https://doi.org/10.1029/TC008i005p01079.
Mora, A., Casallas, W., Ketcham, R.A., Gomez, D., Parra, M., Namson, J., Stockli, D., Almendral, A., Robles, W., Ghorbal, B., 2015. Kinematic restoration of contractional basement structures using thermokinematic models: a key tool for petroleum system modelling. Am. Assoc. Pet. Geol. Bull. 99, 1575–1598. https://doi.org/10.1306/04281411108.
Müller, J.P., Kley, J., Jacobshagen, V., 2002. Structure and Cenozoic kinematics of the Eastern Cordillera, southern Bolivia (21°S). Tectonics 21https://doi.org/10.1029/2001TC001340. 1-1-1–24.
Olsen, J.E.S., McQuarrie, N., Robinson, D.M., 2019. Determining kinematic order and relative age of faulting via flexural-kinematic restoration: a case study in far western Nepal. Basin Res. https://doi.org/10.1111/bre.12362.
Oncken, O., Hindle, D., Kley, J., Elger, K., Victor, P., Schemmann, K., 2006. Deformation of the central Andean upper plate system—Facts, fiction, and constraints for plateau models., in: O. Oncken, et al. (Ed.), The Andes—Active Subduction Orogeny. Springer-Verlag, Berlin, pp. 3–27. ISBN-13: 9783540243298. doi:10.1007/978-3-540-48684-8_1.
Oncken, O., Boutelier, D., Dresen, G., Schemmann, K., 2012. Strain accumulation controls failure of a plate boundary zone: linking deformation of the Central Andes and lithosphere mechanics. Geochemistry, Geophys. Geosystems 13, 1–22. https://doi.org/10.1029/2012GC004280.
Perez, N.D., Horton, B.K., McQuarrie, N., Stubner, K., Ehlers, T.A., 2016. Andean shortening, inversion and exhumation associated with thin- and thick-skinned deformation in southern Peru. Geol. Mag. 1–29. https://doi.org/10.1017/S0016756816000121.
Rak, A.J., McQuarrie, N., Ehlers, T.A., 2017. Kinematics, exhumation, and sedimentation of the north-central Andes (Bolivia): an integrated thermochronometer and thermokinematic modelling approach. Tectonics 36, 1–31. https://doi.org/10.1002/2016TC004440.
Reiners, P.W., 2005. Zircon (U-Th)/He thermochronometry. Rev. Mineral. Geochemistry 58, 151–179. https://doi.org/10.2138/rmg.2005.58.6.
Reiners, P.W., Farley, K.A., Hickes, H.J., 2002. He diffusion and (U–Th)/He ther- mochronometry of zircon: initial results from Fish Canyon Tuff and Gold Butte. Tectonophysics 349, 297–308. https://doi.org/10.1016/S0040-1951(02)00058-6.
Reiners, P.W., Spell, T.L., Nicolescu, S., Zanetti, K.A., 2004. Zircon (U-Th)/He thermochronometry: He diffusion and comparisons with 40Ar/39Ar dating. Geochim. Cosmochim. Acta 68, 1857–1887. https://doi.org/10.1016/j.gca.2003.10.021.
Royden, L.H., 1993. The tectonic expression slab pull at continental convergent boundaries. Tectonics 12, 303–325. https://doi.org/10.1029/92TC02248.
Ryan, J., Beck, S.L., Zandt, G., Wagner, L., Minaya, E., Tavera, H., 2015. Central Andean crustal structure from receiver function analysis. Tectonophysics 682, 120–133. https://doi.org/10.1016/j.tecto.2016.04.048.
Saylor, J.E., Horton, B.K., 2014. Nonuniform surface uplift of the Andean plateau revealed by deuterium isotopes in Miocene volcanic glass from southern Peru. Earth Planet. Sci. Lett. 387, 120–131. https://doi.org/10.1016/j.epsl.2013.11.015.
Schellart, W.P., 2017. Andean mountain building and magmatic arc migration driven by subduction-induced whole mantle flow. Nat. Commun. 8, 1–13. https://doi.org/10.1038/s41467-017-01847-z.
Sempere, T., 1995. Phanerozoic evolution of Bolivia and adjacent regions. In: Tankard, A.J., Suarez, R., Welsink, H.J. (Eds.), Petroleum Basins of South America: AAPG Memoir 62, pp. 207–230 ISBN: 0891813411.
Sempere, T., Butler, R.F., Richards, D.R., Marshall, L.G., Sharp, W., Swisher, C.C., 1997. Stratigraphy and chronology of Upper Cretaceous-lower Paleogene strata in Bolivia and northwest Argentina. Bull. Geol. Soc. Am. 109, 709–727. https://doi.org/10.1130/0016-7606(1997)109<0709:SACOUC>2.3.CO;2.
Sempere, T., Carlier, G., Soler, P., Fornari, M., Carlotto, V., Jacay, J., Arispe, O., Néraudeau, D., Cárdenas, J., Rosas, S., Jiménez, N., 2002. Late Permian-Middle Jurassic lithospheric thinning in Peru and Bolivia, and its bearing on Andean-age tectonics. Tectonophysics 345, 153–181. https://doi.org/10.1016/S0040-1951(01)00211-6.
Springer, M., 1999. Interpretation of heat-flow density in the Central Andes. Tectonophysics 306, 377–395. https://doi.org/10.1016/S0040-1951(99)00067-0.
Stockmal, G.S., Beaumont, C., Nguyen, M., Lee, B., 2007. Mechanics of thin-skinned fold-and-thrust belts: insights from numerical models. Geol. Soc. Am. Spec. Pap. 433, 63–98. https://doi.org/10.1130/2007.2433(04).
Sundell, K.E., Saylor, J.E., Lapen, T.J., Horton, B.K., 2019. Implications of variable late Cenozoic surface uplift across the Peruvian central Andes. Sci. Rep. 1–12. https://doi.org/10.1038/s41598-019-41257-3.
Suppe, J., 1983. Geometry and kinematics of fault-bend folding. Am. J. Sci. 283, 684–721. https://doi.org/10.2475/ajs.283.7.684.
Tawackoli, S., 1999. Andine Entwicklung der Ostkordillere in der Region Tupiza (Südbolivien). 203. Selbstverlag Fachbereich Geowissenschaften, FU, Berlin, pp. 1–116.
Turcotte, D.L., Schubert, G., 1982. Geodynamics. John Wiley, New York (ISBN13: 9780471060185).
Uba, C.E., Heubeck, C., Hulka, C., 2005. Facies analysis and basin architecture of the Neogene Subandean synorogenic wedge, southern Bolivia. Sediment. Geol. 180, 91–123. https://doi.org/10.1016/j.sedgeo.2005.06.013.
Uba, C.E., Kley, J., Strecker, M.R., Schmitt, A.K., 2009. Unsteady evolution of the Bolivian Subandean thrust belt: the role of enhanced erosion and clastic wedge progradation. Earth Planet. Sci. Lett. 281, 134–146. https://doi.org/10.1016/j.epsl.2009.02.010.
Whipp, D.M., Ehlers, T.A., Braun, J., Spath, C.D., 2009. Effects of exhumation kinematics and topographic evolution on detrital thermochronometer data. J. Geophys. Res. Earth Surf. 114, 1–20. https://doi.org/10.1029/2008JF001195.
Whipple, K.X., Gasparini, N.M., 2014. Tectonic control of topography, rainfall patterns, and erosion during rapid post-12 Ma uplift of the Bolivian Andes. Lithosphere 6, 251–268. https://doi.org/10.1130/L325.1.
Williams, K.E., 1995. Tectonic Subsidence Analysis and Paleozoic Paleogeography of Gondwana, in: Tankard, A.J., Suarez S., R., Welsink, H.J. (Eds.), Petroleum Basins of South America: AAPG Memoir vol. 62. pp. 79–100. (ISBN: 0891813411).
Wobus, C.W., Whipple, K.X., Kirby, E., Snyder, N., Johnson, J., Spyropolou, K., Crosby, B., Sheehan, D., 2006. Tectonics from topography: procedurses, promise, and pitfalls. In: Willett, S.D., Hovius, N., Brandon, M.T., Fisher, D.M. (Eds.), Tectonics, Climate, and Landscape Evolution: Geological Society of America Special Paper. Penrose Conference Series, vol. 398. pp. 55–74. https://doi.org/10.1130/2006.2398(04).
Wolfe, M.R., Stockli, D.F., 2010. Zircon (U-Th)/He thermochronometry in the KTB drill hole, Germany, and its implications for bulk He diffusion kinetics in zircon. Earth Planet. Sci. Lett. 295, 69–82. https://doi.org/10.1016/j.epsl.2010.03.025.